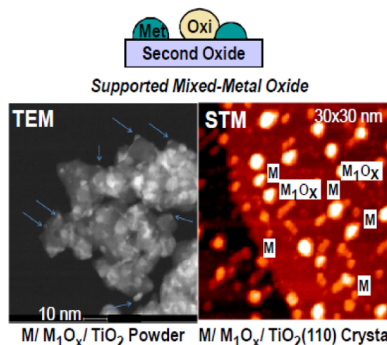


Fundamental Studies of Well-Defined Surfaces of Mixed-Metal Oxides: Special Properties of $\text{MO}_x/\text{TiO}_2(110)$ {M = V, Ru, Ce, or W}

Darío J. Stacchiola, Sanjaya D. Senanayake, Ping Liu, and José A. Rodriguez*

Chemistry Department, Brookhaven National Laboratory, Upton, New York 11973, United States



CONTENTS

1. Introduction	4373
1.1. Supported Mixed-Metal Oxides vs Bulk Mixed-Metal Oxides	4373
1.2. Scope of the Review	4374
2. $\text{VO}_x/\text{TiO}_2(110)$	4374
2.1. Vanadium Oxide Monolayer Catalysts	4374
2.2. Dimers and Clusters of Vanadia on $\text{TiO}_2(110)$	4374
2.3. Selective Oxidation of Methanol	4376
3. $\text{RuO}_x/\text{TiO}_2(110)$	4377
3.1. Photocatalytic Activity of Ru-Modified TiO_2 Powders	4377
3.2. Nanowires of RuO_x Stabilized on $\text{TiO}_2(110)$	4377
3.3. Low-Temperature CO Oxidation	4378
4. $\text{CeO}_x/\text{TiO}_2(110)$	4379
4.1. Highly Reducible Supported Ceria	4379
4.2. Ce^{3+} Dimers on $\text{TiO}_2(110)$	4380
4.3. Water–Gas Shift Reaction	4382
4.4. Photocatalytic Water Splitting under Visible Light	4384
5. $\text{WO}_x/\text{TiO}_2(110)$	4386
5.1. Properties of WO_3/TiO_2	4386
5.2. Isolated WO_3 Trimers on $\text{TiO}_2(110)$	4386
6. Conclusions	4388
Author Information	4388
Corresponding Author	4388
Notes	4388
Biographies	4388
Acknowledgments	4389
References	4389

1. INTRODUCTION

1.1. Supported Mixed-Metal Oxides vs Bulk Mixed-Metal Oxides

Mixed-metal oxides play a very important role in many areas of chemistry, physics, and materials science.^{1–5} The combination

of two metals in an oxide matrix can produce materials with novel structural or electronic properties which can lead to a superior performance in technological applications. In general, there is a need to obtain a fundamental understanding of the phenomena associated with the behavior of these complex systems. For many years there has been a strong interest in studying the behavior of mixed-metal oxide catalysts.^{6–19} Mixed-metal oxides are active catalysts for selective hydrogenation and isomerization of olefins, water–gas shift (WGS) reaction, dehydrogenation of alcohols, oxidation of CO and alkanes, NO reduction, SO_2 destruction, photolysis of water, etc.^{20–22} In principle, several phenomena can contribute to the superior performance of these complex systems, and scientific criteria are very much needed for choosing the “right” combination of elements when designing a mixed-metal oxide catalyst. In a traditional catalyst, metal nanoparticles are dispersed over an oxide support, with the presumption that the main role of the support is to stabilize and disperse the metal particles along its surface. Typically, there is a low concentration of chemically active sites in the oxide, and these may be blocked by the anchoring of the metal particles. By using a second oxide as a support (host), one can create a multifunctional configuration in which the catalyst exposes metal nanoparticles and chemically active oxide nanoparticles to the reactants (see Figure 1). Thus, the reactants can interact with defect sites of the oxide nanoparticles, metal sites, and metal–oxide interfaces. The activity of the catalyst will depend on how all these different elements of the system are combined. Similarly to the well-established higher activity of metal nanoparticles with respect to their bulk phase, deposition of an oxide on submonolayer amounts over a second oxide host can create nanostructures which in turn may enhance the overall catalytic properties of the entire system. One of the first clear observations of this effect was reported in 1946, where the maximum activity of a $\text{MoO}_x/\text{Al}_2\text{O}_3$ catalyst was observed for a monolayer of molybdena. However, the concept of monolayer catalysts did not become popular until the 1980s, in particular with the study of monolayer vanadia catalysts. Bond and Tahir wrote one of the first extensive reviews on this field,²³ recognizing that unique oxo species different from those found at the surface of the bulk oxides could be formed and stabilized. Characterization of these oxo species is a very challenging task. Established experimental techniques used for characterization of powder catalysts cannot easily differentiate the reactive oxo species formed on the surface of monolayer catalysts. Advancements on strategies and development of surface-

Special Issue: 2013 Surface Chemistry of Oxides

Received: August 2, 2012

Published: December 4, 2012

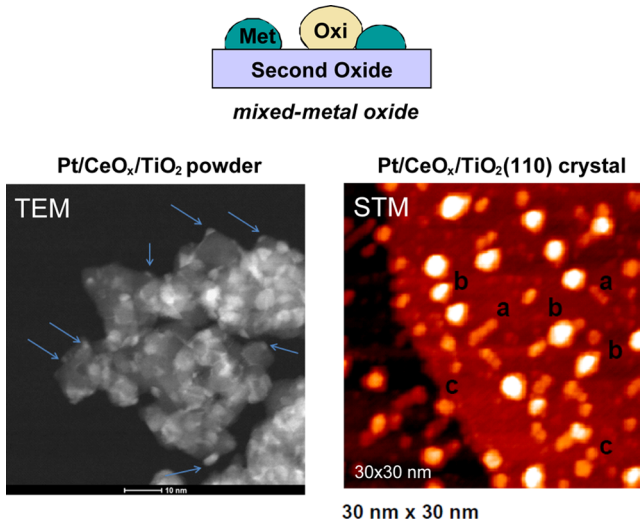


Figure 1. (Top) Typical configuration of a mixed-metal oxide catalyst with nanoparticles of a metal and an oxide codeposited on the surface of a second (host) oxide. (Bottom left) TEM image for a Pt/CeO_x/TiO₂ powder catalyst.²⁵ Arrows denote the position of ceria particles on top of the titania substrate. Small particles of Pt (0.4–0.5 nm) are difficult to detect with TEM. (Bottom right) STM image for a Pt/CeO_x/TiO₂(110) catalyst.²⁶ Labels denote nanoparticles of CeO_x on titania (a), Pt on CeO_x (b), and Pt on titania (c).

sensitive techniques to address monolayer catalysts have recently been reviewed.²⁴

1.2. Scope of the Review

At the left side of Figure 1 is shown a transmission electron microscope (TEM) image for a highly active Pt/CeO_x/TiO₂ catalyst.²⁵ The loading of Pt is very low (0.5 wt %), and the small particles of the metal (0.4–0.5 nm) are difficult to detect with TEM. The TiO₂ support nanoparticles are monocrystalline and present an average size of 10–15 nm. The bright spots, as indicated by the arrows, represent CeO₂ nanoparticles with an average diameter of about 4–5 nm. In the Pt/CeO_x/TiO₂ catalyst, the very low content of Pt points to the need for characterization techniques with high sensitivity.²⁵ Furthermore, since the surface morphology of the powder catalyst is highly heterogeneous, it is difficult to perform detailed mechanistic studies on this system and to explore possible correlations between surface structure or composition and chemical reactivity. For fundamental studies, it may be advantageous to work with a Pt/CeO_x/TiO₂(110) model catalyst.²⁶ In the scanning tunneling microscopy (STM) image in the right side of Figure 1 one can identify three types of structures.²⁶ The surface contains nanoparticles of CeO_x with a wire-like structure and a height close to 1.4 Å (labeled a). On top or near ceria structures, there are bright features with a height in the range of 4–9 Å that correspond to Pt particles in direct contact with ceria (labeled b). Finally, there are small round features that have a height in the range of 3–5 Å, which are not seen in STM images for CeO_x/TiO₂(110), and probably correspond to Pt particles on top of the TiO₂(110) substrate (labeled c).²⁶ Spectroscopic and catalytic tests indicate that the powder Pt/CeO_x/TiO₂ and Pt/CeO_x/TiO₂(110) systems have a high concentration of Ce³⁺ sites at the ceria/titania interface and both are highly active for catalyzing the WGS shift reaction (CO + H₂O → CO₂ + H₂),^{26,27} but in the case of Pt/CeO_x/TiO₂(110) one can take advantage of the large arsenal of characterization techniques

that have been developed in the area of surface science in the last 30 years.²⁸ Furthermore, when coupling experiment and theory,²⁹ computational modeling of Pt/CeO_x/TiO₂(110) is much easier than modeling of the Pt/CeO_x/TiO₂ powder catalyst.²⁶ In general, the combination of theoretical calculations with experiments on well-defined single-crystal surfaces has been a quite useful approach for explaining the behavior of mixed-metal oxides and providing a conceptual frame for dealing with these materials.^{13,18,26,29–32}

In this article, we give an overview of recent work focused on investigating the properties of clusters or nanoparticles of VO_x, RuO_x, CeO_x, and WO_x on TiO₂(110). Mixed-metal oxide catalysts which contain submonolayer amounts of VO_x, RuO_x, CeO_x, or WO_x dispersed on titania are quite important in industrial applications,^{1,4,6,13,22,28,33} and the TiO₂(110) substrate is one of the most studied oxide surfaces.³⁴ As we will show below, experiments with a well-defined substrate allow better control of the structural or morphological properties of the mixed-metal oxides, making feasible a systematic study of these systems. Thus, one can explore relationships between their structural, electronic, and chemical properties and improve the understanding of the more complex powder catalysts. Experiments using the modern techniques of surface science are giving exciting insights into phenomena responsible for the behavior of mixed-metal oxides at the nanometer range.^{12,13,15,28} The ability to control the structure of a mixed-metal oxide at the nanometer level opens new approaches for the design of novel catalysts.

2. VO_x/TiO₂(110)

2.1. Vanadium Oxide Monolayer Catalysts

Vanadia submonolayers or monolayers supported on oxides such as titania, ceria, zirconia, alumina, or silica are known to be excellent catalysts for selective oxidation reactions.^{6,8,13,22,23,32,33} Despite numerous studies, determination of the exact structure for the vanadia species in these mixed-metal oxides remains a challenging task.^{6,14,22,32,33} Interestingly, the submonolayer or monolayer films of vanadia exhibit a higher activity or selectivity than the unsupported oxide material.^{6,14,22} Thus, V₂O₅/TiO₂ is a superior catalyst to the unsupported V₂O₅ for partial oxidation of many hydrocarbons and for selective catalytic reduction (SCR) of nitric oxide.^{35,36} As shown in Figure 2, the amount of vanadia deposited on titania has a drastic effect on the catalytic activity and selectivity of the system.³⁷ Although the mechanism by which titania modifies the properties of the supported vanadia has been the subject of many investigations,^{6,14,22,32,33,38–44} questions still remain about the nature of the active phase and how it is formed. The surface structure of the catalyst depends on the vanadia concentration and the nature of the interface bonds between the vanadia and the titania support.^{6,23} The oxides of vanadium include VO, V₂O₃, VO₂, V₂O₅, and a wide range of intermediate phases.^{6,23,28,41} In the literature, there is unanimity that vanadia sites might be present on the surface of the titania support in three different forms as a function of the degree of isolation: Isolated monomeric VO₄ species with tetrahedral coordination (Figure 3A), one or two-dimensional oligomeric species connected by V–O–V bridges (Figure 3B), and three-dimensional bulk vanadium oxides (amorphous or crystalline).⁶

2.2. Dimers and Clusters of Vanadia on TiO₂(110)

The atoms protruding in the O-briging rows of stoichiometric TiO₂(110) are ideal for binding V or VO_x species.^{28,45} X-ray

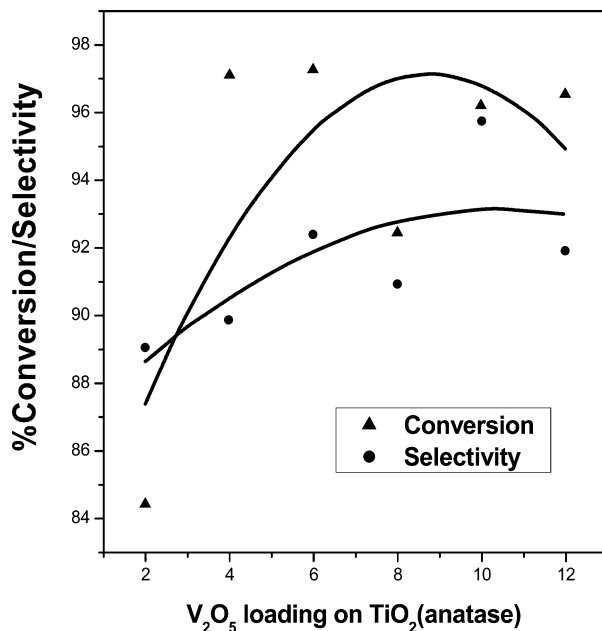


Figure 2. Conversion and selectivity for ammonoxidation of 3-picoline over a V₂O₅/TiO₂ catalysts as a function of V₂O₅ loading (reaction temperature, 633 K).³⁷

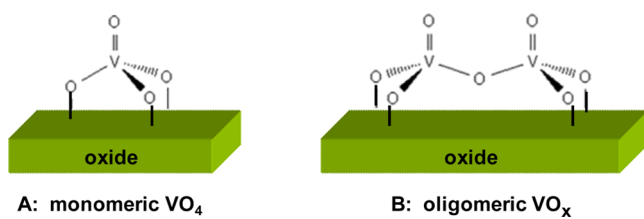


Figure 3. Two typical configurations for vanadia supported on oxide surfaces.

photoelectron spectroscopy (XPS), ultraviolet photoelectron spectroscopy (UPS), metastable impact electron spectroscopy (MIES), near-edge X-ray absorption fine structure spectroscopy (NEXAFS), and scanning tunneling microscopy (STM) have been used to study the electronic properties of V atoms and VO_x clusters on TiO₂(110).^{10,35,28,38,45} A strong interaction has been observed between V atoms and the stoichiometric TiO₂(110) surface.^{10,35} Adsorbed V attacks the surface Ti–O bonds violently. The (1 × 1) LEED pattern observed on the TiO₂(110) surface completely disappears at V coverages below 0.5 ML.³⁵ STM images indicate that at very small coverages of V the adatoms sit near atoms in the bridging oxygen rows, see Figure 4.⁴⁵ Deposition of vanadium onto TiO₂(110) at room temperature leads to a marked decrease in the work function. This decrease has been interpreted as a consequence of the transformation of Ti⁴⁺ → Ti³⁺ and oxidation of V driven by the high affinity of vanadium for oxygen.^{10,35,40} Theoretical calculations for V/TiO₂(110) predict a net V → TiO₂ electron transfer that oxidizes V and produces Ti³⁺ sites in the titania substrate.^{32,33} The degree of oxidation of V depends on the admetal coverage and the conditions used for deposition. At very low coverages, V^{3+/4+} species have been reported based on XPS data showing a V 2p_{3/2} peak at 516.2 eV.^{35,44} At higher coverages, V^{2+/3+} species were formed with a broad V 2p_{3/2} peak at 514.6 eV and particles 10–15 Å in diameter were observed. The corresponding reduction of the substrate was

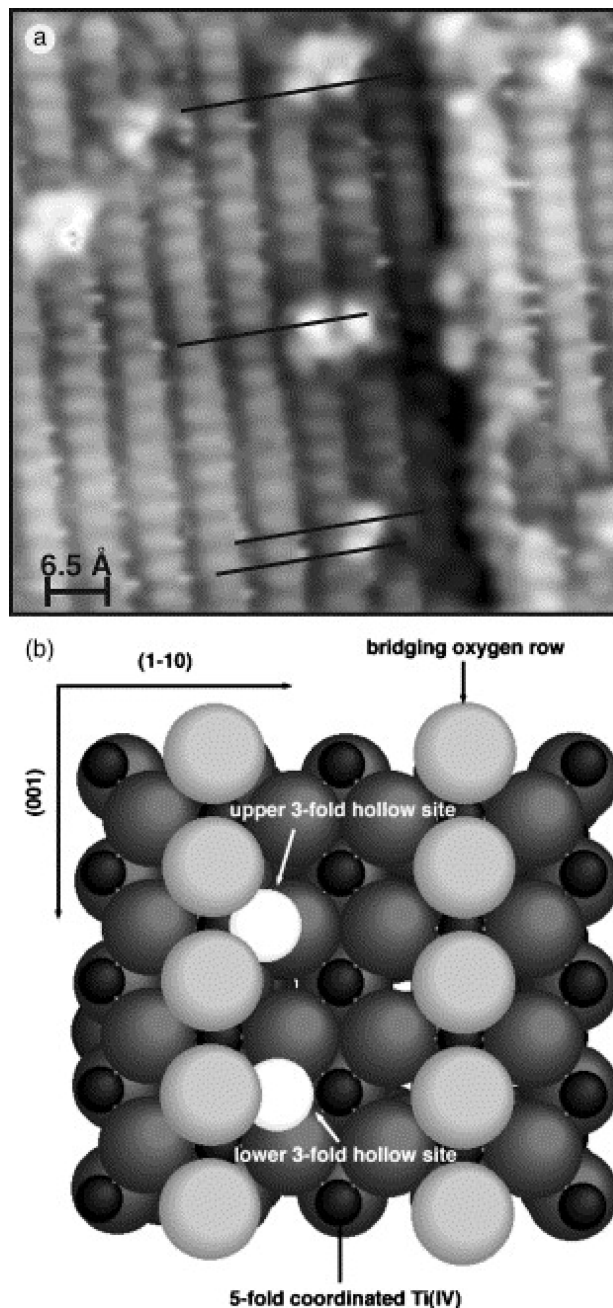


Figure 4. (a) STM image of 0.05 ML V on TiO₂(110) (67 Å × 67 Å; 1.77 V, 1.07 nA).⁴⁵ Thin lines on the image indicate the registry of the V adatoms with respect to the maxima on the bright Ti rows. (b) Model of the V/TiO₂(1 1 0) surface, top view. Reprinted with permission from ref 45. Copyright 2003 Elsevier.

confirmed by the appearance of Ti³⁺ features in XPS spectra. With the addition of vanadium a feature appears between 0.5 and 2 eV in the valence region and is usually assigned to occupied V 3d and Ti 3d states.^{10,35} A very different behavior was found for V adsorption onto reduced TiO₂(110) surfaces. In these cases, there was no significant change in the work function upon V deposition and the V 2p core-level binding energies were close to that of metallic V, even at low V coverages. The model that results from these observations is that there is only a weak interaction at the V–TiO₂ interface.^{28,35} Since the reduced surface is deficient in O

atoms the V adatoms are forced to interact primarily with Ti cations and are unable to bond to O ions.^{28,35}

In general, vanadia can be deposited on $\text{TiO}_2(110)$ following two different methodologies. In one approach, vanadium is first deposited on the TiO_2 crystal and then oxidized in an O_2 atmosphere. In a second approach, vanadium is deposited under a background atmosphere of O_2 . It has been found that the reactive evaporation technique produces more uniform and better-ordered vanadia layers than the postoxidation method.¹¹ Vanadia films in the submonolayer-to-multilayer coverage regime were deposited on $\text{TiO}_2(110)$ at 300 K by evaporation of metallic vanadium in an environment of O_2 and studied by XPS and NEXAFS. Photoemission data point to formation of a vanadium oxide with partially filled d orbitals.^{35,38,44} The position and line shape of the vanadium L and oxygen K edges determined by NEXAFS for vanadia particles indicate V_2O_3 formation. The titanium L edge indicates only a weak interaction of V_2O_3 with the surface of titania which is also implied by the results of XPS measurements. The geometry of the $\text{V}_2\text{O}_3/\text{TiO}_2(110)$ system has been examined by X-ray photoelectron diffraction (XPD).⁴⁶ The structure of the V_2O_3 overlayer does not match that of bulk-like corundum V_2O_3 , being more similar to a strongly oxygen-defective rutile structure.⁴⁵ Theoretical calculations have shown that several subsurface sites involving Ti substitution by V are more stable than any on-surface adsorption site for vanadium atoms.⁴⁰ This process of $\text{Ti} \leftrightarrow \text{V}$ substitution probably involves a substantial activation barrier. Annealing of $\text{V}_2\text{O}_3/\text{TiO}_2(110)$ to temperatures above 1100 K leads to formation of a ternary oxide at the interface and simultaneous agglomeration of V_2O_3 .⁴¹

Depending on the choice of oxide deposition parameters (oxygen pressure, substrate temperature, and V evaporation rate), practically all bulk oxide phases of V can be prepared on $\text{TiO}_2(110)$: VO ,⁴⁷ V_2O_3 ,^{48,49} VO_2 ,^{50,51} and V_2O_5 ,^{52,53} but no conclusive evidence of formation of monomers has yet been reported. The morphology of some of these oxide overlayers have been studied using STM.¹¹ When low coverages of V were deposited under an oxygen atmosphere (1×10^{-8} mbar) at 473 K, small bright features with an apparent mean height of ~ 3.5 Å and 10–15 Å long were observed predominantly on top of the 5-fold-coordinated Ti rows (Figure 5).¹¹ These features are probably dimers of vanadia. Accurate analysis of the topography of these structures (inset of Figure 5) shows two protrusions located on the different crystallographic sites: One follows the correct epitaxial stacking and occupies a bridge position between two titanium atoms, while the other site sits on top of a 5-fold-coordinated titanium atom.¹¹ At a coverage of 0.6 ML, some agglomeration of the vanadia clusters was visible, with preferential coalescence of the clusters along the substrate [001] direction.¹¹ This tendency continued when the vanadia coverage was increased to 1 ML, where strands running parallel to the [001] direction were formed. At 2 ML the TiO_2 surface was almost completely covered by the vanadia strands.¹¹ On the basis of results of XPD^{11,17} and angle-resolved photoemission fine structure (ARPEFS),¹⁷ the strands in the STM images have been assigned to strands of a rutile-type VO_2 phase (there are very few differences between the lattice parameters of VO_2 and those of TiO_2), which in some regions may be decorated by finely dispersed clusters of a higher V–oxide phase.¹¹

In addition to the studies for VO_x on $\text{TiO}_2(110)$, vanadia particles have been deposited on well-defined surfaces of ceria, alumina, and tin oxide.^{13,54–59} STM and infrared reflection

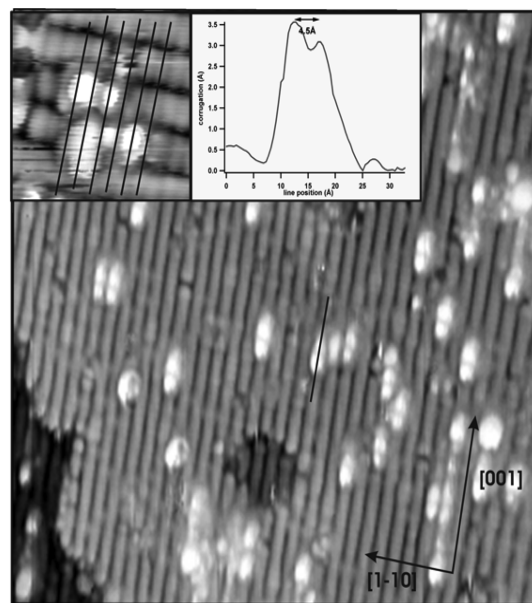


Figure 5. STM image of 0.2 ML V–oxide deposited on $\text{TiO}_2(110)$ at 473 K by reactive evaporation in 5×10^{-8} mbar of O_2 ($200 \text{ \AA} \times 200 \text{ \AA}$; 1.964 V, 0.633 nA). (Inset) Line-scan across a vanadia dimer along the [001] direction.¹¹ Reprinted with permission from ref 11. Copyright 2004 Elsevier.

absorption spectroscopy (IRAS) have been used to study the growth of vanadia on a well-ordered alumina film formed by oxidation of the (110) surface of a NiAl alloy.⁵⁵ In the low-coverage regime the vanadia overlayer appears as homogeneously distributed small particles with diameters in the range of 20–30 Å. IRAS shows the presence of $\text{V}=\text{O}$ groups localized either at the particle surface or at its interface with the alumina. Interface-localized vibrations involving V, O, and Al ions have also been detected.⁵⁸ The interaction of vanadia clusters or nanoparticles with $\text{CeO}_2(111)$ has been examined using photoelectron spectroscopy (PES), IRAS, TPD, STM, and density-functional (DF) calculations.^{13,57–59} STM images show that highly dispersed species are formed upon deposition of vanadium onto $\text{CeO}_2(111)$ under an atmosphere of O_2 .¹³ The images indicate the existence of vanadyl monomers positioned atop protrusions in the ceria substrate. The corresponding IR spectrum gives a vanadyl ($\text{V}=\text{O}$) stretching vibration at 1006 cm^{-1} .¹³ IR spectroscopy results suggest that the vanadia monomers observed by STM are positioned with the vanadyl group perpendicular to the surface, which has been confirmed by the results of DF calculations.¹³

2.3. Selective Oxidation of Methanol

The terminal $\text{V}=\text{O}$ bonds present in VO_x/TiO_2 and other mixed-metal oxide surfaces have been proposed by many investigators to contain the active oxygen involved in oxidation reactions over supported vanadia catalysts.^{6,22,32,41} Experimental and theoretical studies have shown that the $\text{V}=\text{O}$ bonds in $\text{VO}_x/\text{TiO}_2(110)$ do affect the chemical properties of the surface.^{33,60} Figure 6 displays the calculated structure for the adsorption of water on a fully oxidized $\text{VO}_x/\text{TiO}_2(110)$ surface. The results of the DF calculations indicate that the system is stabilized by formation of H bonds between the water protons and the adjacent vanadyl oxygens. The appropriate vanadyl oxygen $\text{V}=\text{O}$ is shifted from the plane $\text{V}=\text{O}=\text{V}$. Such a configuration initiates breaking of the water O–H bond and

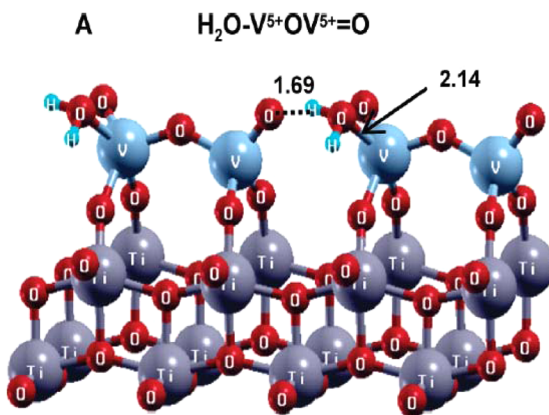


Figure 6. Calculated adsorption geometry for water on a fully oxidized $\text{VO}_x/\text{TiO}_2(110)$ surface.³³

hydrogen transfer to form a hydroxylated VO_x/TiO_2 surface.³³ In a similar way, terminal $\text{V}=\text{O}$ bonds could help in the cleavage of $\text{O}-\text{H}$ bonds in simple alcohols or other OH-containing hydrocarbons. Reaction of methanol on $\text{TiO}_2(110)$ -supported vanadium oxide was studied using temperature-programmed desorption (TPD) and high-resolution electron energy loss spectroscopy (HREELS).⁶⁰ TPD results show that methanol is oxidized to formaldehyde on monolayer and submonolayer vanadia films on $\text{TiO}_2(110)$, whereas both clean $\text{TiO}_2(110)$ and multilayer vanadia films supported on $\text{TiO}_2(110)$ are relatively inactive for this reaction. Figure 7

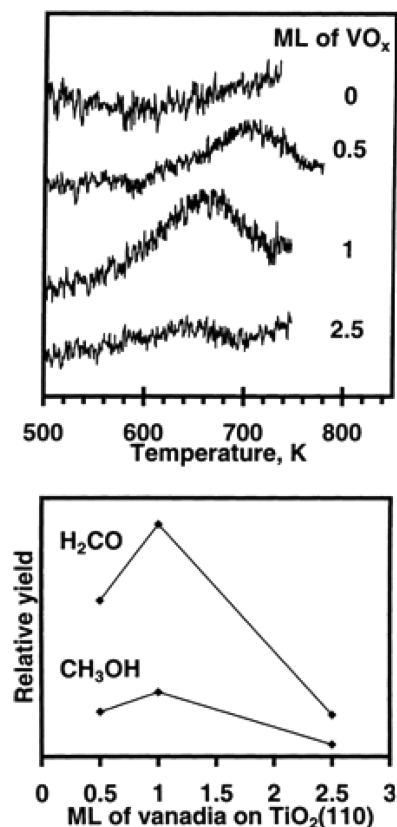


Figure 7. (Upper panel) H_2CO desorption spectra from CH_3OH -dosed $\text{VO}_x/\text{TiO}_2(110)$ samples for various vanadia coverages. (Lower panel) Relative yields of H_2CO and CH_3OH in the TPD spectra as a function of vanadia coverage.⁶⁰

shows the result of TPD experiments for adsorption of methanol on $\text{TiO}_2(110)$ samples covered by 0.5, 1, and 2.5 ML of vanadia.⁶⁰ The area of the H_2CO peak varies with vanadia coverage and goes through a maximum near 1 ML. Only a very small H_2CO peak was detected in the spectrum from the 2.5 ML vanadia film, indicating that multilayer vanadia films are nearly inactive for oxidation of methanol to formaldehyde. HREELS results demonstrate that methoxides are the primary surface intermediates in the oxidation of methanol to formaldehyde on the supported vanadium layers. The reactivity trends obtained for the model catalysts used in this study are similar to those observed for high surface area analogues. This suggests that vanadia films supported on single-crystal metal oxide substrates are excellent model systems for studying the relationships between the structure and the reactivity of supported oxide catalysts.⁶⁰

3. RuO_x/TiO₂(110)

3.1. Photocatalytic Activity of Ru-Modified TiO₂ Powders

Recently, there has been strong interest in understanding the role of mixed-metal oxides in catalysts used for production of hydrogen through the splitting of water. In this respect the $\text{RuO}_2/\text{TiO}_2$ system has received much attention. Several studies have shown that the TiO_2 decorated with RuO_2 particles or films could catalyze oxygen production by improving the efficiency of charge separation at the metal–oxide/semiconductor interface.^{61–63} Furthermore, it has been shown that RuO_2 can work also as a good catalyst for hydrogen evolution.⁶¹ Ru-modified TiO_2 exhibits photocatalytic activity under visible light due to formation of an impurity energy level which then modifies the band gap of TiO_2 .⁶³ Also, it has been reported that ruthenium oxide caused the anatase to rutile transformation to occur at lower temperatures, resulting in a decrease in the band gap.⁶² Thus, a literature survey indicates that there is controversy on the role of Ru/RuO_x in enhancing the photocatalytic activity of TiO_2 , and moreover, there is a clear need to understand the water dissociation pathway on these mixed-metal oxide surfaces.^{64,65} Structural and chemical properties of $\text{RuO}_x/\text{TiO}_2(110)$ surfaces were investigated employing STM, photoemission, and DF calculations.^{65,66}

3.2. Nanowires of RuO_x Stabilized on TiO₂(110)

Nanowires of RuO_x can be grown on $\text{TiO}_2(110)$ by adsorption and decomposition of $\text{Ru}_3(\text{CO})_{12}$ with subsequent exposure to O_2 at elevated temperature (550–650 K). XPS was used to follow the chemistry of this process. The carbonyl was dosed at 300 K, and all Ru–CO bonds were cleaved when the sample temperature was raised to 600 K, producing a Ru 3d XPS spectrum that matched that of metallic Ru. Ru particles in contact with $\text{TiO}_2(110)$ were very reactive toward molecular oxygen. Exposure to O_2 at 550 K eventually led to a Ru → RuO_x transformation, producing Ru 3d XPS spectra similar to that of bulk RuO_2 .^{65,66} The morphology of the $\text{RuO}_x/\text{TiO}_2(110)$ surfaces was investigated with STM.⁷ The top panel in Figure 8 shows a STM image recorded after depositing on $\text{TiO}_2(110)$ a submonolayer coverage of RuO_2 . The RuO_2 forms one-dimensional (1D) wire-like structures along the $\langle 001 \rangle$ direction of the $\text{TiO}_2(110)$ substrate. The RuO_2 nanowires are well dispersed on the titania and cover this substrate in a uniform way. They have apparent heights in the range of 2.2–3.0 Å; see bottom panel in Figure 8. These heights are consistent with a single layer of RuO_2 in which the Ru cations share O atoms with the Ti cations in the $\text{TiO}_2(110)$ surface. A

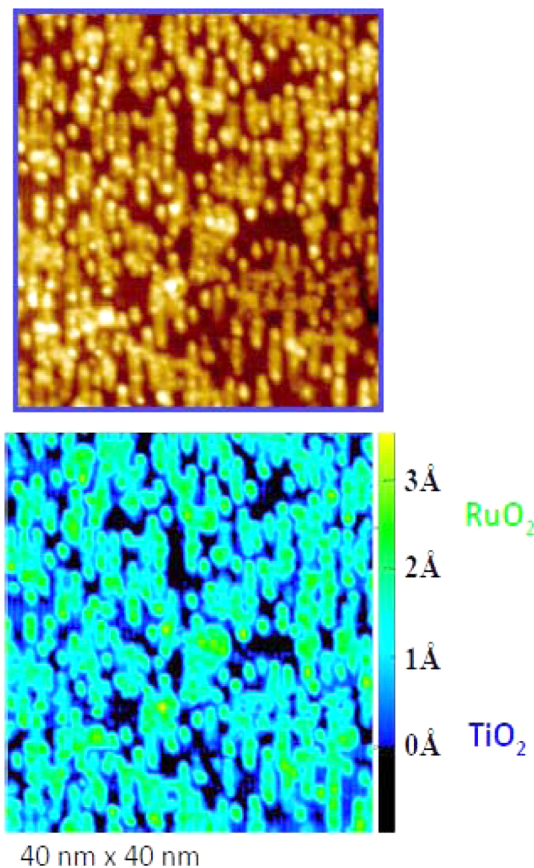


Figure 8. (Top) STM image for a $\text{RuO}_2/\text{TiO}_2(110)$ surface.⁶⁵ Bright wire-like features denote nanostructure of RuO_2 ($V_t = 2.0$ V; $I_t = 1.0$ nA). (Bottom) Multicolor STM image to enhance the contrast between features of different apparent heights.

detailed view of the morphology of $\text{RuO}_x/\text{TiO}_2(110)$ at low coverages of RuO_2 is shown in Figure 9.⁶⁵ On the surface one can see features for O vacancies and O adatoms together with two types of strands that can be easily differentiated by their apparent height and brightness. The dark strands, marked in red boxes, are rare in the surface and have an apparent height of about 1.2 Å. They match well with features of TiO_x obtained after exposing $\text{TiO}_2(110)$ to molecular O_2 at 400–600 K.^{67,68} The high-resolution STM image of the dark strands, red inset in top of Figure 9, exhibits three rows of bright dots running along the $\langle 001 \rangle$ direction. These structural features agree well with those seen within rows of TiO_x generated in studies for $\text{O}_2/\text{TiO}_2(110)$.^{67,68} In contrast, the bright strands (marked with white or black boxes in Figure 9) have heights (2.2–3.0 Å) not seen for TiO_x rows on $\text{TiO}_2(110)$. They correspond to RuO_2 or a mixture of RuO_2 and TiO_x rows. In images of high resolution (top of Figure 9), the bright strands of RuO_2 display a single row of bright spots centered in the strand. STM images indicate that the center of a RuO_2 nanowire is aligned with the cusp-Ti rows of the $\text{TiO}_2(110)$ substrate, and this wire (or strand) has an apparent width of about 9 Å.

DF calculations were used to investigate several possible structures for RuO_x on $\text{TiO}_2(110)$. The structure shown in Figure 10 exhibited high stability and was in excellent agreement with the images found with STM, showing that each RuO_2 wire covers three rows of the $\text{TiO}_2(110)$ substrate and exhibits bright protrusions at the wire center probably as a consequence of a row of oxygen atoms located above Ru

atoms.^{65,66} The wire-like structures of RuO_2 on top of $\text{TiO}_2(110)$ were very reactive toward water dissociation, being able to cleave O–H bonds at a temperature as low as 200 K. The calculated barrier for dissociation of water on RuO_2 nanowires is <0.05 eV. The presence of easily formable O vacancies in the ruthenium oxide nanowires led to spontaneous dissociation of water, Figure 11. Furthermore, $\text{RuO}_2/\text{TiO}_2(110)$ was able to catalyze production of hydrogen through the WGS reaction ($\text{H}_2\text{O} + \text{CO} \rightarrow \text{H}_2 + \text{CO}_2$) exhibiting an activity that compares well with the activity found for extended surfaces of copper typically used as benchmarks to study this reaction.⁶⁵

A combination of statistical thermodynamics and DF results was used to take into account the effect of temperature, oxygen pressure, and ruthenium concentration on the stability of the ruthenium oxide wires on the $\text{TiO}_2(110)$ surface.⁶⁶ Calculations suggest that as the temperature increases under UHV, the RuO_2 wires become unstable and should start to lose oxygen at temperatures above 500 K. This is in agreement with results of XPS and STM which show the disappearance of the RuO_x wires at elevated temperatures and formation of Ru nanoparticles. The $\text{RuO}_x \leftrightarrow \text{Ru}$ transformation is completely reversible. Temperature and oxygen pressure had a dramatic effect on the elemental composition and morphology of the $\text{RuO}_x/\text{TiO}_2(110)$ systems.⁶⁶ Interestingly, the RuO_x nanostructures in contact with titania lose oxygen at much lower temperatures (700–850 K) than bulk RuO_2 (>1000 K).⁶⁹ This property must be taken into consideration when preparing $\text{RuO}_x/\text{TiO}_2$ catalysts since it can lead to big changes in catalytic activity or selectivity. In fact, this characteristic of $\text{RuO}_x/\text{TiO}_2$ may be the cause for the controversy that exists in the literature about the intrinsic activity of this material in photocatalytic processes.^{62–65}

3.3. Low-Temperature CO Oxidation

The high reactivity of $\text{RuO}_x/\text{TiO}_2(110)$ toward CO and O_2 makes this system an excellent catalyst for oxidation of CO.⁶⁶ Figure 12 compares the CO oxidation activity of $\text{TiO}_2(110)$, $\text{RuO}_2/\text{TiO}_2(110)$, and $\text{Au}/\text{TiO}_2(110)$ surfaces at 350 K. Under these reaction conditions, relatively low temperature, and a stoichiometric ratio of CO and O_2 , neither $\text{TiO}_2(110)$ nor $\text{RuO}_2(110)$ is an active catalyst.^{70,71} In contrast, titania surfaces covered 15–25% by RuO_2 exhibit activities comparable to the maximum activity of $\text{Au}/\text{TiO}_2(110)$, which is an excellent catalyst for CO oxidation.^{15,71} This is remarkable since ruthenium is considerably less expensive than gold. Table 1 shows DF-calculated reaction energy changes (ΔE) for CO oxidation on $\text{TiO}_2(110)$ and on a model $\text{RuO}_2/\text{TiO}_2(110)$ surface.⁶⁶ On $\text{TiO}_2(110)$, one finds a CO adsorption energy of only –0.19 eV and the reaction energy for formation of CO_2 is endothermic by 1 eV. In contrast, on the $\text{RuO}_2/\text{TiO}_2(110)$ surface, the adsorption energy of CO on a five-coordinated Ru site is –1.1 eV and the reaction energy for formation of CO_2 is exothermic by 0.8 eV. The special structural properties of $\text{RuO}_x/\text{TiO}_2(110)$ favor dissociative adsorption of O_2 ($\Delta E = -2.99$ eV) and easy release of oxygen present in the RuO_x lattice, making this surface an excellent catalyst for oxidation processes.

When compared to other systems that contain oxide nanoparticles dispersed on well-defined oxide substrates { VO_x on $\text{TiO}_2(110)$ or $\text{CeO}_2(111)$,^{11,13} $(\text{WO}_3)_3$ on $\text{TiO}_2(110)$,¹² CeO_x on $\text{TiO}_2(110)$ ^{15,16}}, one finds that, in spite of the high stability of bulk RuO_2 , $\text{RuO}_x/\text{TiO}_2(110)$ is the only mixed-

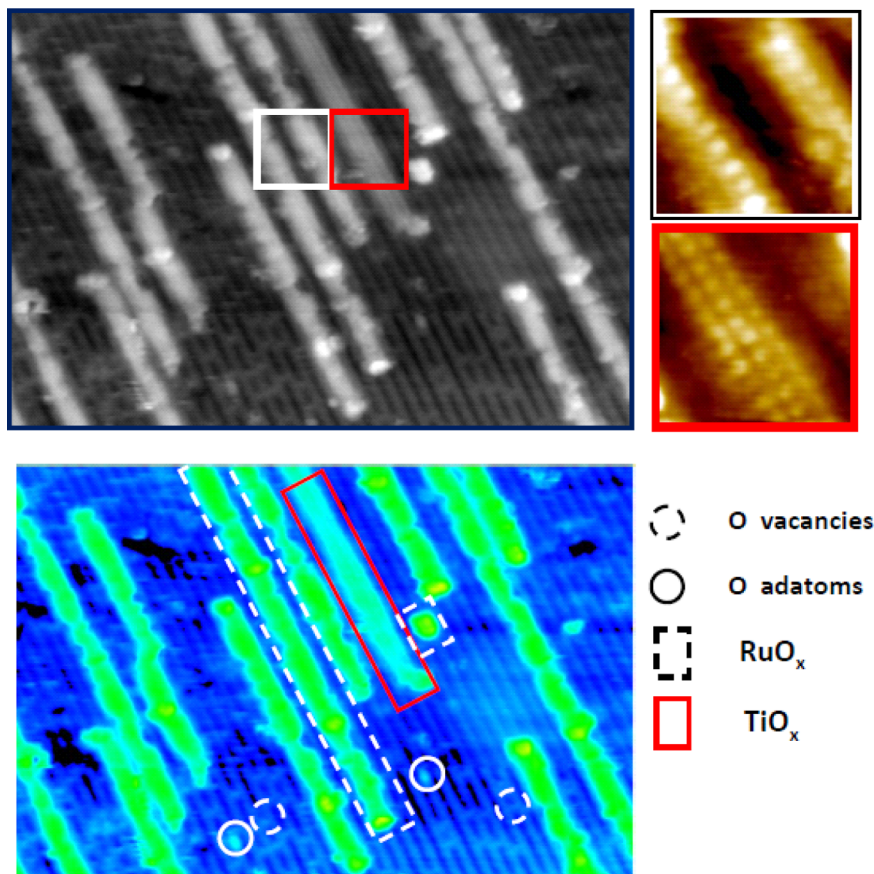


Figure 9. (Top) STM image for a small coverage of RuO₂ on TiO₂(110) {30 nm × 20 nm; V_t = 1.5 V; I_t = 1.2 nA}.⁶⁵ Insets in the right side magnify in detail the structures of RuO₂ (white or black boxes) and TiO_x (red boxes). (Bottom) Color map for the relative heights of RuO₂ nanowires with respect to the TiO₂(110) surface. Correspondence between color and height is the same as that shown in Figure 8.

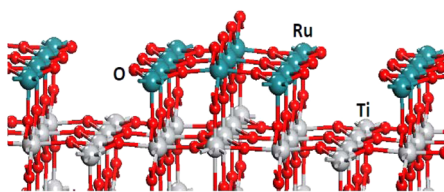


Figure 10. DFT-calculated structure for RuO₂ nanowires on TiO₂(110).⁶⁵

metal oxide system in which the oxide overlayer is easily reduced to a metallic state.⁶⁶ Thus, by taking advantage of the complex interactions that occur in a mixed-metal oxide at the nanometer level, one can engineer materials that have unique chemical properties.

4. CeO_x/TiO₂(110)

4.1. Highly Reducible Supported Ceria

The ability of CeO₂ to undergo reduction and reoxidation is important for a number of catalytic applications.^{4,14,15,43} The performance of ceria in automotive catalysts and fuel cells can be enhanced by doping this oxide with a second metal (M = Zr, Ca, V, Cu, Au, Pt, Tb, La, Mn, etc.).⁴ The improvement in the catalytic properties of ceria is likely associated with an enhancement in the reducibility of the oxide. One particularly interesting system is that of ceria–titania solutions, with several recent reports indicating that titania doping leads to improved reducibility.⁷² Ceria–titania solutions with compositions of

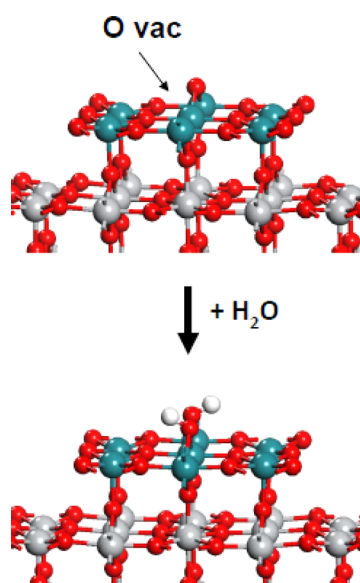


Figure 11. Spontaneous dissociation of water on a RuO_x/TiO₂(110) surface.⁶⁵ OH group forms on the site of an O vacancy.

Ce_{0.9}Ti_{0.1}O₂ and Ce_{0.8}Ti_{0.2}O₂ exist as single-phase, fluorite structures.⁷³ These mixed-metal oxides are shown to be significantly more reducible than bulk ceria, with enthalpies for reoxidation being approximately -119 kcal/mol O₂, compared to -182 kcal/mol O₂ for bulk ceria.⁵¹ A DF study

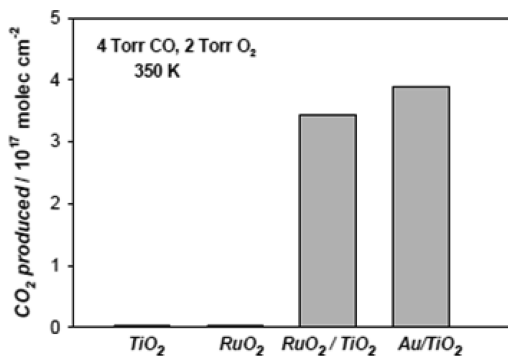


Figure 12. Comparison of the activity for CO oxidation of clean TiO₂(110), a TiO₂(110) surface covered ~18% by RuO₂, and a TiO₂(110) surface with ~0.3 monolayers of Au.⁶⁶ XPS showed Ru⁴⁺ before and after CO oxidation.

Table 1. Energy Changes (ΔE) Calculated (DF-GGA) for the CO + 0.5O₂ → CO₂ Reaction on TiO₂(110) and RuO₂/TiO₂(110) Surfaces⁶⁶

reaction	ΔE (eV)
TiO ₂ (110) + CO → TiO ₂ (110)-Ovac + CO ₂	1.01
TiO ₂ (110)-Ovac + 0.5O ₂ → TiO ₂ (110)	-4.81
RuO ₂ /TiO ₂ (110) + CO → RuO _x /TiO ₂ (110) + CO ₂	-0.81
RuO _x /TiO ₂ (110) + 0.5O ₂ → RuO ₂ /TiO ₂ (110)	-2.99

examined the reducibility of ceria doped with Zr⁴⁺, Hf⁴⁺, Ti⁴⁺, and Th⁴⁺ ions and found that ceria doped with Ti⁴⁺ was the most easily reduced of these mixed-metal oxides.⁴⁶ Ti⁴⁺ cations decreased substantially the O vacancy formation energy in ceria. Lattice parameters for the bulk ceria–titania oxides are shifted only slightly from those of pure ceria, but the Ti⁴⁺ cations embedded in the host oxide exhibit a complex bonding configuration.^{45,74} TiO₂ prefers the rutile/anatase structures rather than the fluorite structure of CeO₂.⁷⁵ For Ce_{0.9}Ti_{0.1}O₂ and Ce_{0.8}Ti_{0.2}O₂, Ti incorporation into the fluorite lattice leads

to a 4-fold tetrahedron-like environment around Ti⁴⁺ by displacing one-half of the oxygen ions toward the Ti⁴⁺ and one-half away from Ti⁴⁺. This leads to an ordered superstructure, closely related to the original fluorite structure, created by a cubic sublattice of Ti⁴⁺ ions and a separated cubic sublattice of displaced oxygen ions.^{45,46} There is a high degree of strain in the lattices of bulk Ce_{0.9}Ti_{0.1}O₂ and Ce_{0.8}Ti_{0.2}O₂.

4.2. Ce³⁺ Dimers on TiO₂(110)

What happens when ceria nanoparticles are deposited on titania? Deposition of Ce atoms or CeO_x clusters on a TiO₂(110) substrate produces structures which are very different from those of bulk ceria or ceria nanoparticles supported on metal surfaces or silica films (Figure 13).^{76–80} Less than 0.1 ML of Ce atoms were deposited on a clean TiO₂(110) surface at room temperature in UHV to investigate the interactions between metallic Ce and titania.¹⁵ In measurements of XPS and UPS, the oxidation state of the Ti cations changed from +4 to +3 and Ce was found in a +3 oxidation state (Figure 14). The adsorbed Ce partially reduces the TiO₂ surface by donating electrons to Ti cations. Since the heats of formation of cerium oxides are larger than those of titanium oxides,⁸¹ the titania substrate is forced to share its oxygens with the Ce adatoms. Results of STM and DF calculations suggest that each Ce adatom interacts with two bridging and one in-plane O atoms of the TiO₂(110) surface.^{15,16} The fact that three electrons move from high to lower energy levels, Ce(5d¹6s²) → 3Ti(3d¹), leads to a very high adsorption energy for Ce on TiO₂(110).

The presence of O₂ in the background drastically affected the growth mode of ceria and the morphology of the surface. The left panel in Figure 13 shows a STM image obtained after depositing Ce on the TiO₂(110) surface at 600 K in O₂ (~1 × 10⁻⁷ Torr), and the sample was subsequently annealed to 900 K still under an O₂ environment. The image was taken after cooling the sample down to room temperature and removing the O₂ from the background. The diagonal arrays have a

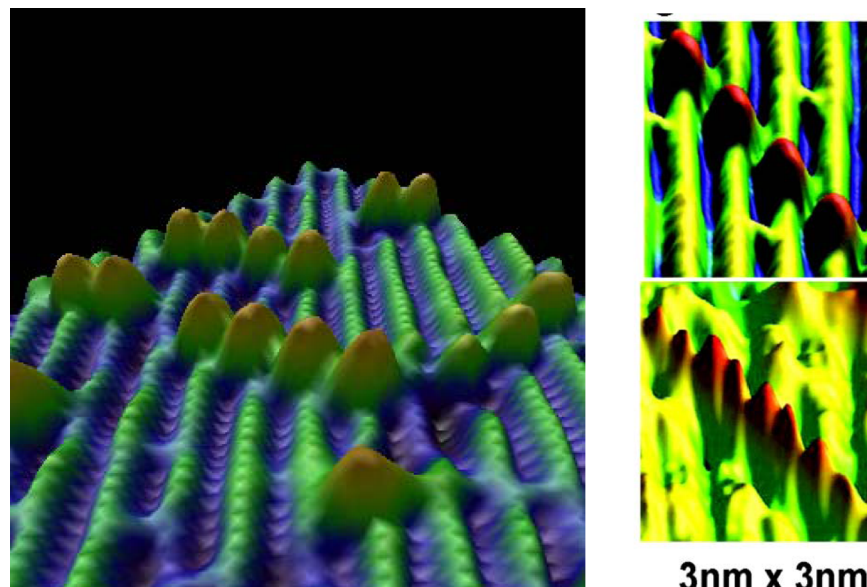


Figure 13. (A) STM image of CeO_x on the TiO₂(110) surface after depositing Ce atoms at 600 K in O₂ ($P_{O_2} = 1 \times 10^{-7}$ Torr) and subsequent annealing at 900 K in O₂ ($P_{O_2} = 1 \times 10^{-4}$ Torr, $V_t = 1.2$ V, $I_t = 0.07$ nA). (B) High-resolution STM image for a low coverage of CeO_x on TiO₂(110). (C) Bias-dependent STM images of a diagonal array of CeO_x nanoparticles taken at the imaging bias of 1.2 V, 0.06 nA (top) and 0.4 V, 0.06 nA (bottom). Ce atoms were dosed at 600 K in O₂ ($P_{O_2} = 5 \times 10^{-5}$ Torr), and subsequently, the sample was annealed to 900 K (taken from ref 16).

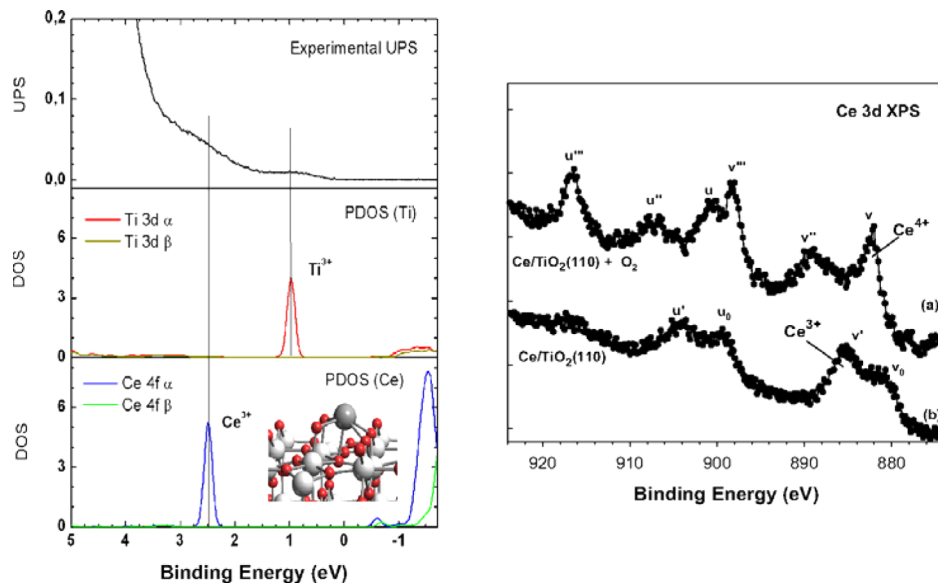


Figure 14. Electronic properties of CeO_x/TiO₂(110). (Left, top) UPS spectrum. Features marked by vertical lines are not seen on clean stoichiometric TiO₂(110). (Left middle and bottom) Displayed are DFT-calculated density of states (DOS) for a Ce/TiO₂(110) surface. Color code for spheres: gray, cerium; red, oxygen; white, titanium. (Right) Ce 3d XPS spectra taken after depositing Ce on TiO₂(110) at 298 K (bottom), with subsequent exposure to 1 Torr of O₂ (top).¹⁵

distinctive height (~ 1.4 Å) and correspond to CeO_x nanoparticles.^{15,16} To better understand the structures of the CeO_x nanoparticles, a bias-dependent STM measurement was performed as shown in the left panel in Figure 13. These two images display the same diagonal arrays of CeO_x nanoparticles but obtained at different imaging bias. The top STM image was taken with an imaging bias of +1.2 V, and the angle of the diagonal array is close to 42° with respect to the [1–10] direction. When this feature was imaged at +0.4 V, the individual bright features appeared as dimers. Each ceria dimer is located between two rows of oxygens protruding from the surface. XPS spectra indicated that the oxidation state of the Ce atoms in the dimers was essentially +3. Titanium cations were mainly Ti⁴⁺ with a small amount (<5%) of Ti³⁺ comparable to that found on clean TiO₂(110).

DF calculations were used to study the bonding configuration of the ceria dimers on TiO₂(110). A Ce atom interacts with two bridging and one in-plane O atoms of the titania surface. Starting with this structure, dissociation of an O₂ molecule near the adsorbed Ce is a highly exothermic process and an energy of 6.88 eV is released.¹⁶ If a second Ce atom is deposited on this surface, the CeO₂ monomer would be an excellent binding site to create a dimer. At the end, the ceria dimer adopts a configuration comparable to the STM images in Figure 13 and has an oxidation state of +3, without generation of Ti³⁺ species, as seen in the XPS measurements.¹⁶ Overall, DF calculations show that Ce₂O₃ particles are stabilized as mixed-metal oxide on the surface of TiO₂ compared to the bulk phase, while CeO₂ is destabilized. As a result, the TiO₂-supported ceria clusters can be much easier to be oxidized or reduced than the bulk materials. To better understand the different stability between these phases, the DOS projected on Ce and O atoms in both bulk and supported-particle phases for Ce₂O₃ and CeO₂ were calculated.⁸² The density of states (DOS) for the isolated free particle with the same geometry as the supported particle has also been included for comparison, in order to determine the effect of the structure of the nanoparticle and the effect of the interaction with the support. As shown in Figure 15,

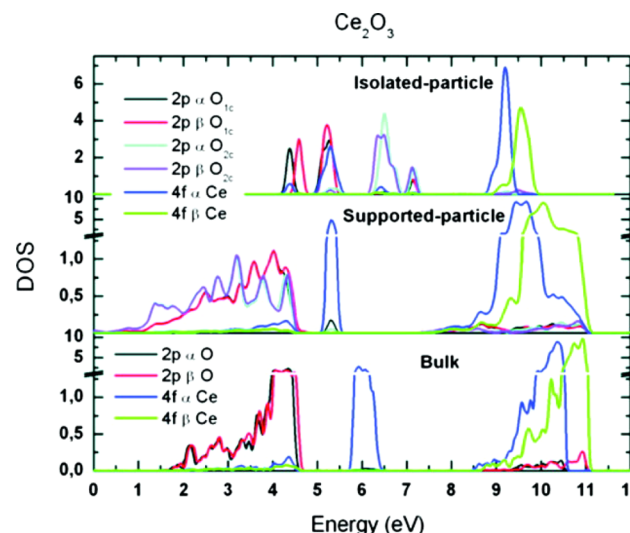


Figure 15. DOS projected on Ce and O atoms of the Ce₂O₃ unit for the systems: perfect bulk (bottom), supported particle on TiO₂(110) (middle), and isolated particle with the same geometry as that of the supported one (top). O1c and O2c stand for oxygen atoms mono- and bicoordinated to Ce atoms, respectively.⁸²

formation of the mixed-metal oxide involves significant changes in the electronic structure of ceria. For the free particle, molecular bands with strongly mixed Ce 4f and O 2p were observed, indicating a high degree of covalent bonding, that is, the isolated Ce₂O₃ unit is electronically transformed into a molecule. However, when this particle is deposited on TiO₂, the electronic structure of the particle returns to a solid-like DOS with wide O 2p and Ce 4f bands. The effect of the interaction with the support is very important since it “crystallizes” the electronic structure of the cerium oxide particle from an initial “molecular” distribution, leading to a true mixed-metal oxide rather than a supported particle.

The surface in Figure 13 can be used as a model to study the catalytic behavior of mixed-metal oxide supports.¹⁵ CeO_x

nano particles drastically affect the growth mode of Au, Cu, and Pt on $\text{TiO}_2(110)$.^{15,16} On this surface, the admetals grow forming three-dimensional particles. Gold exhibits very weak interactions with the ideal terraces of $\text{TiO}_2(110)$ ⁸³ and mainly binds to defects or step sites.^{71,84} Deposition of Au at room temperature, ~0.2 ML, produced three-dimensional metal particles anchored to steps of the titania surface, to the (1 × 2) reconstructions of $\text{TiO}_2(110)$, and to the CeO_x dimers.¹⁵ On $\text{CeO}_x/\text{TiO}_2(110)$, the dispersion of the Au was substantially larger than that seen on a pure $\text{TiO}_2(110)$ surface where Au mainly binds to the steps.^{71,84} The trends for Au/ $\text{CeO}_x/\text{TiO}_2(110)$ are similar to those found after depositing small coverages of Cu or Pt on $\text{CeO}_x/\text{TiO}_2(110)$ ¹⁶ or Au on $\text{CeO}_x/\text{SiO}_2$.⁸⁰ CeO_x sites are essential for nucleation of small particles of the admetals on terraces of the oxide support.

4.3. Water–Gas Shift Reaction

Neither $\text{CeO}_x/\text{TiO}_2(110)$ nor Au(111) is able to catalyze CO oxidation ($\text{CO} + 0.5\text{O}_2 \rightarrow \text{CO}_2$) or the WGS reaction ($\text{CO} + \text{H}_2\text{O} \rightarrow \text{H}_2 + \text{CO}_2$). However, Au/ $\text{CeO}_x/\text{TiO}_2(110)$ surfaces proved to be outstanding catalysts.^{15,16} Figure 16 compares the

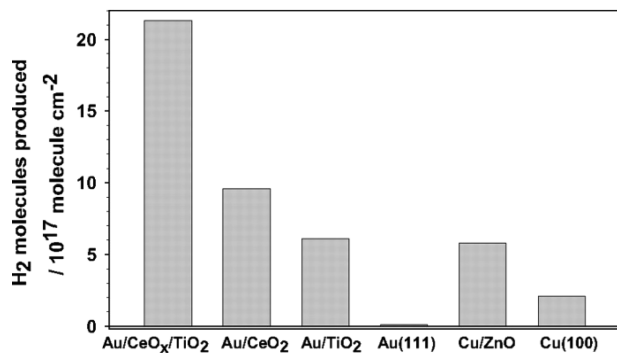


Figure 16. Comparison of the water–gas shift activity of Cu(100), Au(111), and 0.5 mL of Au supported on $\text{TiO}_2(110)$, $\text{CeO}_2(111)$, or $\text{CeO}_x/\text{TiO}_2(110)$. Data for Cu(100), Cu/ZnO(0001), and Au/ $\text{CeO}_2(111)$.¹⁵

WGS activity of Au/TiO₂(110) and Au/CeO_x/TiO₂(110) surfaces as a function of Au coverage. The Au/TiO₂(110) systems are good WGS catalysts,⁸³ but they did not come close to matching the activity of Au/CeO_x/TiO₂(110). The same is valid when comparing to the WGS activities of Au/ $\text{CeO}_2(111)$,⁸⁵ CeO_x/Au(111), Cu/ZnO(0001), and copper single crystals.^{15,86} Cu/ZnO is the most common WGS catalyst used in industry,⁸⁷ and copper is the best pure metal catalyst.^{86,88} For the Au/CeO_x/TiO₂(110) catalysts, one could assume that the concentration of active sites is proportional to the number of ceria regions in contact with gold nanoparticles. Since only 12% of the titania support was covered by ceria, as measured by ion scattering spectroscopy (ISS), the Au/CeO_x/TiO₂(110) catalyst must be at least 300 times more active than a Cu(100) surface on a per active-site basis.^{15,85} Even more active WGS catalysts are found after depositing Cu and Pt on CeO_x/TiO₂(110). In the M/CeO_x/TiO₂(110) (M = Cu, Au, Pt) systems, there is a strong coupling of the chemical properties of the admetal and the mixed-metal oxide. Figure 17 shows the WGS activity of Pt/TiO₂(110) and two sets of Pt/CeO_x/TiO₂(110) catalysts in which 11% or 23% of the titania substrate was covered by ceria particles. Figure 1 shows a representative STM image of these Pt/CeO_x/TiO₂(110) model catalysts, where it is clearly observed that

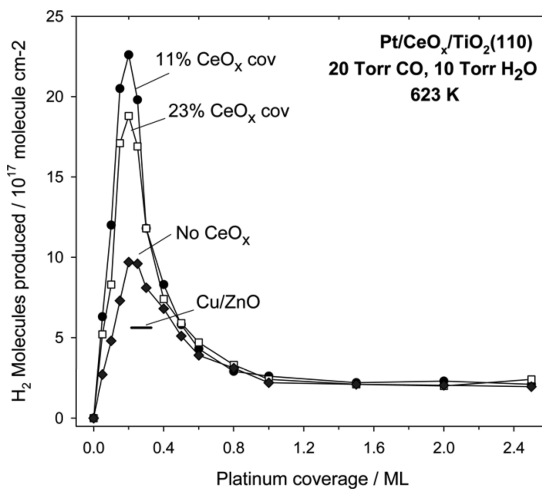


Figure 17. WGS activities of model Pt/TiO₂(110) and Pt/CeO_x/TiO₂(110) catalysts as a function of admetal coverage. Before vapor deposition of the Pt, ceria was dispersed on TiO₂(110) covering 11% and 23% of this substrate. Each surface was exposed to a mixture of 20 Torr CO and 10 Torr H₂O at 625 K for 5 min. Maximum activity found for the WGS reaction on the Cu/ZnO(0001) system ($\theta_{\text{Cu}} = 0.5$ ML) has been included for comparison.²⁶

ceria acts as a preferred nucleation center for Pt nanoparticles. The fraction of titania covered by ceria was measured using ISS¹⁵ before deposition of the Pt. Maximum activities were seen for catalysts containing a small amount of Pt ($\theta_{\text{Pt}} < 0.3$ ML) and ceria (11% of the titania covered). These systems did not show signs of deactivation with time after kinetic tests of up to 2 h. The estimated turnover frequencies for catalysts containing 0.15 ML of Pt were 34.8 (11% of titania covered by ceria) and 28.6 (23% of titania covered by ceria) molecules Pt_{site}⁻¹ s⁻¹. For this small Pt coverage, the Pt/CeO_x/TiO₂(110) catalysts were ~3 times more active than the corresponding Pt/CeO₂(111) catalyst. On the other hand, at large coverages of Pt (>0.8 ML), when most of the metal adatoms are not affected by interactions with ceria and the Pt exhibits a large density of Sd states near the Fermi level, the catalytic activities of the Pt/CeO_x/TiO₂(110) and Pt/CeO₂(111) systems are very close and similar to that of bulk Pt.

Cu/ZnO catalysts are frequently used in industrial processes for production of hydrogen via the WGS reaction.⁸⁷ Pt/CeO_x/TiO₂ exhibits a WGS activity substantially higher than those of Cu/ZnO(0001)⁸⁵ and Pt/TiO₂, Pt/CeO₂, and clean Pt(111).⁸⁹ Pt gets activated by electronic interactions with ceria, and these Pt ↔ CeO_x interactions seem to be stronger when one has small platinum and ceria nanoparticles. Dissociation of water is frequently the rate-determining step for the WGS reaction on metal or metal/oxide surfaces.^{78,86–88} In TPD experiments, it was found that the Pt/CeO_x/TiO₂(110) surfaces were able to dissociate water all the way to yield molecular H₂. DFT calculations also point to facile dissociation of water on small Pt clusters electronically perturbed by interactions with ceria. Studies have been carried out on dissociation of water on Pt(111), on free Pt₇₉ and Pt₈ particles,^{90,91} and at Pt₈–ceria interfaces (see the corresponding structures in Figure 18). These systems were chosen taking into consideration previous studies showing that the activities of very small metal clusters supported on SiO₂ and MgO are very different from that of larger clusters.^{92,93} The Pt₇₉ and Pt₈ particles contain corner and edge atoms that have a coordination number significantly

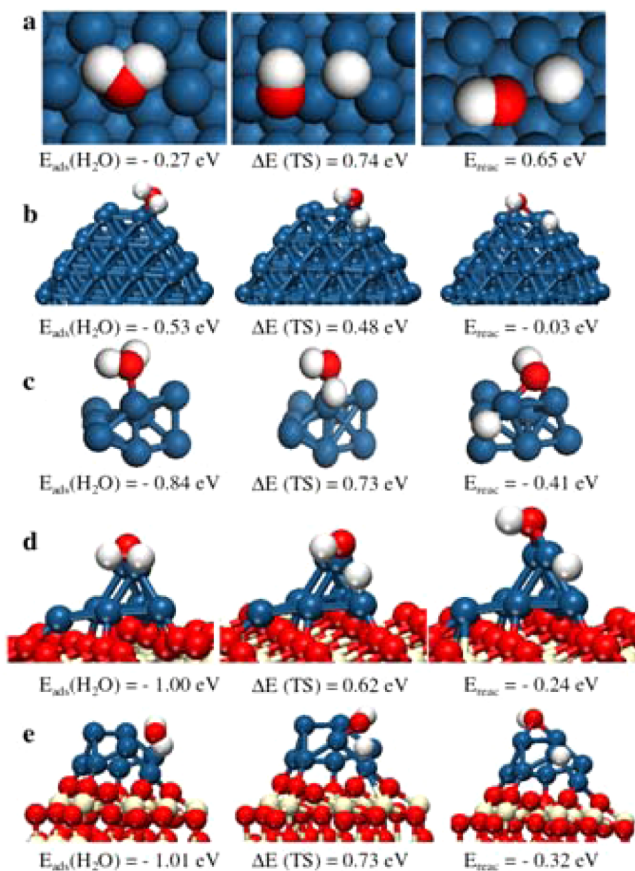


Figure 18. DFT-calculated structures for (left) adsorbed H_2O , (center) the transition state (TS), and (right) adsorbed $\text{HO} + \text{H}$ along with the corresponding energy parameters [E_{ads} , $\Delta E(\text{TS})$, E_{react}] for dissociation of water over (a) a $\text{Pt}(111)$ surface, (b) a free Pt_{79} cluster, (c) a free Pt_8 cluster, and (d and e) Pt_8 clusters deposited on (d) a $\text{CeO}_2(111)$ surface and (e) a $\text{Ce}_{40}\text{O}_{80}$ nanoparticle with a compact structure. Pt, O, Ce, and H atoms are represented as blue, red, cream, and white spheres, respectively.²⁶

smaller than that of the atoms in a $\text{Pt}(111)$ surface. Pt_8 is highly fluxional and undergoes geometrical changes upon bonding of water or after interaction with $\text{CeO}_2(111)$. The atoms of Pt_8 in contact with the $\text{CeO}_2(111)$ surface (Figure 18d) or with the $\text{Ce}_{40}\text{O}_{80}$ nanoparticle (Figure 18e) are strongly bound to the oxygen sites of the oxide support with a net $\text{Pt} \rightarrow \text{ceria}$ charge transfer.^{90,91} The systems studied in Figure 18 allowed us to separate changes in reactivity due to variations in the coordination number of the Pt atoms (obtained by comparing the results for $\text{Pt}(111)$ and Pt_{79} or Pt_8) from changes in reactivity caused by the interaction of Pt with the ceria support (obtained by comparing the results for free Pt_8 and Pt_8 in contact with $\text{CeO}_2(111)$ or the $\text{Ce}_{40}\text{O}_{80}$ nanoparticle).

In the literature of heterogeneous catalysis, it is well known that the reactivity of the Pt/TiO_2 system can be affected by strong metal–support interactions.⁹⁴ These interactions usually deactivate platinum and involve decoration of the surface of the Pt particles with small aggregates of titania after reduction in H_2 at very high temperature (>770 K). This is completely different from the phenomena seen here, where admetal \leftrightarrow oxide electronic interactions significantly enhance the catalytic activity of Pt: $\text{Pt}(111) \ll \text{Pt}/\text{CeO}_2(111) < \text{Pt}/\text{CeO}_x/\text{TiO}_2(110)$. One must look for this type of interaction when designing metal/oxide catalysts that contain Pt. For example, the type of

interaction that occurs on Pt/CeO_2 does not exist when Pt nanoparticles are deposited on surfaces of alumina or silica. Thus, the $\text{Pt}/\text{Al}_2\text{O}_3$ and Pt/SiO_2 systems exhibit WGS activities that are 10–20 times smaller than that of Pt/CeO_2 and comparable to that of clean $\text{Pt}(111)$.

The high catalytic activity of $\text{M}/\text{CeO}_x/\text{TiO}_2(110)$ can be attributed to the special chemical properties of the Ce_2O_3 dimers supported on titania. Usually the rate-determining step in the WGS reaction is dissociation of water. The Ce^{3+} sites present in $\text{CeO}_x/\text{TiO}_2(110)$ easily dissociate water,¹⁶ but upon exposure to CO, highly stable HCO_x species are formed on the oxide surface, and there is no production of H_2 or CO_2 gas. The $\text{M}/\text{CeO}_x/\text{TiO}_2(110)$ systems are bifunctional catalysts:^{15,16} Adsorption and dissociation of water takes place on the oxide, CO adsorbs on metal nanoparticles, and all subsequent reaction steps occur at oxide–metal interfaces. The results in Figure 16 illustrate the tremendous impact that an optimization of the chemical properties of nanoceria can have on the activity of a WGS catalyst. This has been verified in experiments with high surface area powder $\text{Pt}/\text{CeO}_x/\text{TiO}_2$ catalyst, which in many aspects show a behavior similar to that seen for $\text{Pt}/\text{CeO}_x/\text{TiO}_2(110)$ surfaces.⁹⁵ The approach should be valid in general for catalysts which contain ceria as part of a mixed-metal oxide, opening new directions for tuning catalytic activity by coupling appropriate pairs of oxides. The key issue is to take advantage of the complex interactions that occur in a mixed-metal oxide at a nanometer level. The $\text{VO}_x/\text{CeO}_2(111)^{13}$ and $\text{CeO}_x/\text{TiO}_2(110)^{15}$ systems illustrate two different extremes (ceria as an oxide support and ceria as an oxide overlayer) in which the mixed-metal oxide has a relatively large concentration of Ce^{3+} states and chemical properties substantially different from those of the individual oxides.

The studies described above for $\text{Pt}/\text{CeO}_x/\text{TiO}_2(110)$ have been extended to high surface area powder $\text{Pt}/\text{CeO}_x/\text{TiO}_2$ catalysts in a systematic way, paying particular attention to the properties of the supported ceria and the ceria–titania interface. Powder $\text{Pt}/\text{CeO}_x/\text{TiO}_2$ catalysts were used to generate hydrogen through the water–gas shift reaction or photocatalytic splitting of water with visible light. As mentioned in previous sections, characterization of the interface in $\text{CeO}_2/\text{TiO}_2$ powders is a major challenge because of the complexity and diversity of the structures that can be generated.³¹ Bulk ceria and titania have different crystal structures,^{96–98} but mixing of both oxides is very appealing since exchange of cerium and titanium ions can regulate the bulk and surface physicochemical properties of the resulting material (redox capability, thermal sintering, etc.).^{15,95,98}

Figure 19 shows a TEM image and scanning TEM-electron energy loss spectroscopy (STEM-EELS) results for the same $\text{Pt}/15$ wt % $\text{CeO}_2/\text{TiO}_2$ system as shown in Figure 1. Ce-modified TiO_2 samples ($\text{Ce}-\text{TiO}_2$) were prepared by wet impregnation of the thermally stabilized TiO_2 powders with two different loadings corresponding to one-half and complete theoretical monolayer coverage. The supported-Pt catalysts contain only 0.5 wt % Pt. The TiO_2 support nanoparticles are monocrystalline, mainly with an anatase phase, and have an average size of 10–15 nm. The smaller brighter features are CeO_2 nanoparticles with an average diameter of about 4–5 nm. Pt nanoparticles are barely visible due to their low load and high dispersion, in agreement with the behavior of model catalysts presented above. The EELS spectra shown in Figure 19 allow determination of the $\text{Ce}^{3+}/\text{Ce}^{4+}$ ratio with high spatial resolution within and around the ceria nanoparticles. Ce M

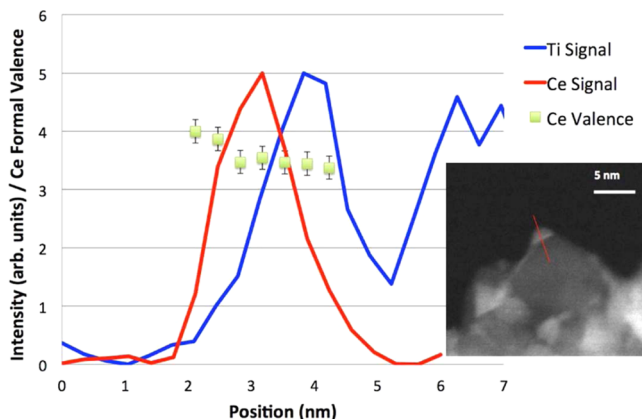


Figure 19. STEM-EELS spectra of Pt/15 wt % $\text{CeO}_2/\text{TiO}_2$ catalyst. Particular ceria nanoparticle used for this measurement is depicted in the inset TEM image. (Red line) Line along which spectra were scanned for EELS signal.²⁵

edges are used to probe f-electrons occupancy in Ce and Ti L edges to probe d-electron occupancy on Ti. On the surface of the CeO_2 particles Ce^{4+} is observed, but as the interface with TiO_2 is approached, a mixed oxide region is observed where Ce^{3+} are stabilized instead.

Two variants of NEXAFS using soft X-rays were employed to further discern the surface and interfacial electronic and chemical states on the $\text{CeO}_2/\text{TiO}_2$ catalysts, and the results are shown in Figure 20. In the partial electron yield (PEY) mode, information from the surface with a depth of less than 2 nm is obtained, because of the small escape depth of secondary or low-energy Auger electrons. Partial fluorescence yield (PFY) measurements of core level absorption edges however gives a near surface sampling depth of about 10 nm. Hence, combination of the two NEXAFS modes of measurement gives access to identify the surface to bulk differences in a catalytic system. Figure 20a shows the PEY Ce M-edge spectra obtained before and after deposition of Pt nanoparticles on bulk CeO_2 powder. The presence of Pt does not change the oxidation state or the structure of bulk ceria. However, the presence of a small concentration of Pt imposes a significant reduction of the CeO_2 nanoparticles dispersed on TiO_2 as observed from both Ce M-edges spectra in Figure 20b and 20c. TEM images in Figures 1 and 19 cannot resolve the presence of Pt aggregates in the $\text{Pt}/\text{CeO}_2/\text{TiO}_2$ system due to their small size, but clearly, a significant fraction of Pt is in close contact with ceria. Figure 21 shows Pt L_{III} EXAFS data for Pt/CeO_2 and $\text{Pt}/\text{Ce-TiO}_2$ catalysts.⁹⁹ Both catalysts have peaks at similar positions (Pt–O distance = 0.105 nm), suggesting the same type of platinum oxide species on these catalysts, which are different from those present in Pt/TiO_2 . These results further advance the hypothesis that the platinum species in the $\text{Pt}/\text{Ce-TiO}_2$ catalysts are preferentially deposited over ceria sites. The preferential nucleation of Pt near the ceria particles is unequivocally established in the studies on model catalysts, as detailed above.

Although Ce_2O_3 is not a stable oxide in the presence of oxygen or an oxidizing environment, studies on model and powder catalysts show that it is possible to stabilize Ce^{3+} cations within a mixed oxide interface such as in $\text{CeO}_x/\text{TiO}_2$. In model studies detailed above, $\text{Pt}/\text{CeO}_x/\text{TiO}_2$ catalysts have shown significantly higher activity for the LT-WGS than the industrial model catalysts.¹⁵ In the case of the powder catalysts,

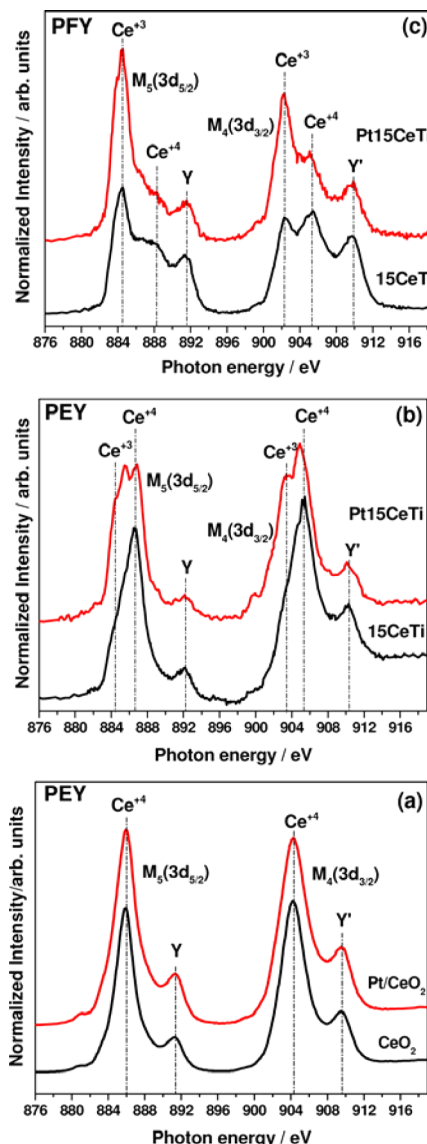


Figure 20. Ce M edges obtained by partial electron yield measurements after depositing 0.5 wt % of Pt on bulk CeO_2 (A) and on a 15 wt % $\text{CeO}_2/\text{TiO}_2$ support (B). (C) Partial fluorescence yield measurements of the Ce M edge of Pt/15 wt % $\text{CeO}_2/\text{TiO}_2$.²⁵

samples with lower Ce content (6 wt % Ce) exhibit higher CO conversion than samples with higher Ce loading (15 wt % Ce). The structural evolution of the catalysts has been followed in situ during the WGS reaction by time-resolved X-ray diffraction (TR-XRD) experiments. Figure 22 shows the changes in cell dimension of the CeO_2 and TiO_2 phases, where an expansion in the cell lattice is observed at 100 °C.²⁷ Expansion is due to a partial reduction of ceria species. Ceria and titania lattices were expanded to a higher degree in the Pt-containing catalysts than on the plain supports. Additionally, the lattice expansion was observed on catalysts at lower temperature with respect to the blank experiments performed over the bare supports. The fact that the changes in both TiO_2 and CeO_2 phases are directly connected suggests that reduction of ceria is aided by TiO_2 under WGS conditions.

4.4. Photocatalytic Water Splitting under Visible Light

TiO_2 has been extensively studied for photochemical reactions but due to its wide band gap does not have any absorption in

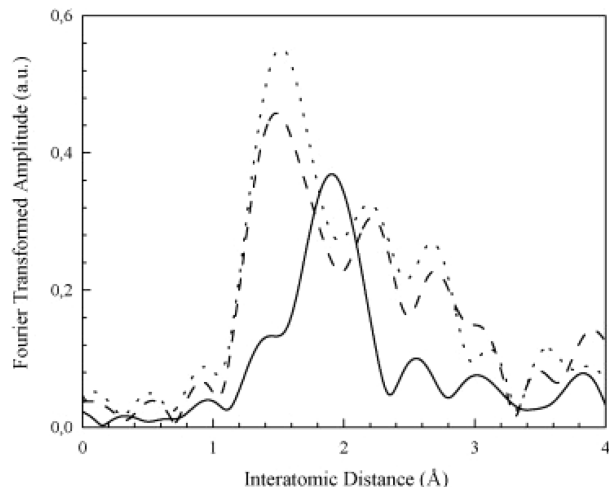


Figure 21. Pt L_{III} edge EXAFS spectra of calcined catalysts: (---) Pt/TiO₂, (—) Pt/Ce-TiO₂, and (...) Pt/CeO₂.⁹⁵ Reprinted with permission from ref 95. Copyright 2010 Elsevier.

the visible range. Modification of titania to increase its chemical and electronic properties is a very active area of research. UV-vis measurements of Pt/CeO_x/TiO₂ samples show that the presence of CeO₂ on the TiO₂ surface enhanced the absorption in the visible range significantly. The photocatalytic activity of Pt dispersed on CeO₂-modified (6 and 15 wt %) TiO₂ under visible was investigated by monitoring O₂ evolution from the system (Figure 23).²⁵ In that study, WO₃ was included as a reference oxide photocatalyst for oxygen evolution from water splitting, as this is used as a benchmark material for oxygen generation.^{100,101} A very small amount of O₂ evolves from the aqueous silver nitrate solution using Pt/TiO₂ as a catalyst under the experimental conditions because when using a cutoff filter of $\lambda \geq 400$ nm a small fraction of UV light is always present in the filtered spectrum causing a small photocatalytic activity. The presence of CeO_x on titania along with Pt significantly improved the O₂ evolution due to formation of a large amount

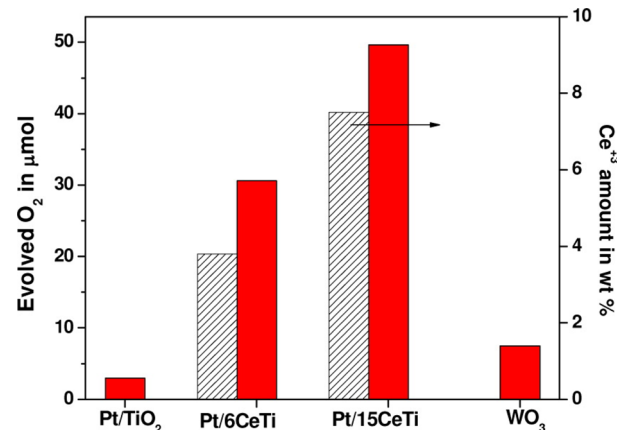


Figure 23. (Left-side axis and red bars) Amount of oxygen evolved on Pt/TiO₂, Pt/CeO_x/TiO₂, and WO₃ catalyst from water photo-oxidation upon visible light ($\lambda > 400$ nm) illumination for 4 h. (Right-side axis) Amount of Ce³⁺ present in the Pt/CeO_x/TiO₂ catalysts calculated from the corresponding Ce M-edge NEXAFS spectra obtained by PEY measurements.²⁵

of Ce³⁺. The Pt/CeO_x/TiO₂ system has about seven times higher activity than the standard WO₃ catalyst and an activity as good as that of the best metal oxide catalysts reported in the literature in recent years for water photo-oxidation under visible light.¹⁰⁰ However, without the presence of Pt, the pure CeO₂/TiO₂ mixed-metal oxide showed a very small activity toward water splitting in visible light. This result indicates that the existence of Ce³⁺ drastically enhances formation of electron–hole pairs, but it does not help to suppress their recombination. The presence of a small amount of Pt is needed in order to act as an electron trap while at the same time increasing the amount of Ce³⁺ as shown above. On the basis of the reported results a possible mechanism for the photocatalytic activity of the Pt/CeO_x/TiO₂ system as shown in Figure 24 can be proposed: Formation of mixed-metal oxides at the interface of the CeO₂ nanoparticles and the TiO₂ support leads to the

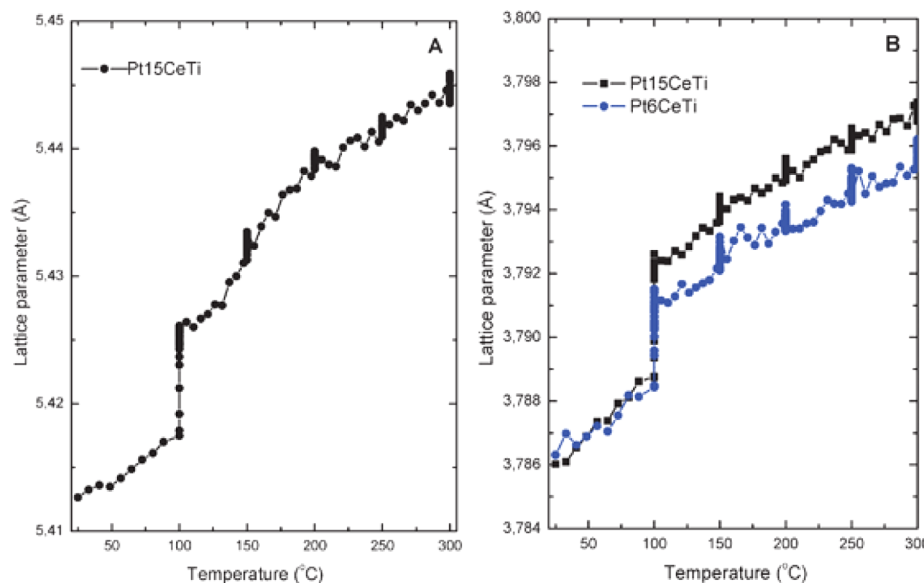


Figure 22. Evolution of the cell dimensions of (A) CeO₂ and (B) TiO₂ phases during WGS reaction over the Pt₆CeTi and Pt₁₅CeTi catalysts (reaction conditions: feed CO = 1 vol %, H₂O/CO = 3, GHSV = 4000 h⁻¹). Cell dimensions are calculated from sequential Rietveld refinement of the time-resolved in situ XRD patterns.²⁷ Reprinted with permission from ref 27. Copyright 2011 Royal Society of Chemistry.

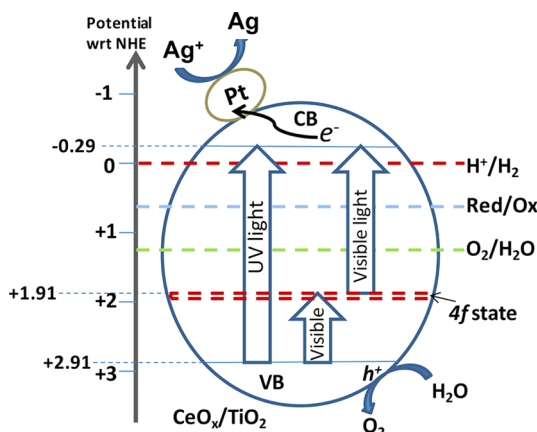


Figure 24. Proposed mechanism for photocatalytic evolution of oxygen from water upon irradiation of Pt/CeO_x/TiO₂.²⁵

presence of a significant amount of reduced cerium. The existence of Ce³⁺ ions generates an extra energy state, belonging to the partially occupied 4f level, between the conduction and valence bands of TiO₂.^{15,16} This generates a reduced band gap of about 2.2 eV in the mixed-metal oxide phase. Visible light now can excite the electrons from the valence band to the intermediate Ce 4f band or from the Ce 4f band to the conduction band, thus forming electron–hole pairs. Electrons then get trapped by Pt nanoparticles and reduce the silver nitrate present in the solution. On the other hand, the holes will oxidize the water to oxygen.

The behavior of Pt/CeO_x/TiO₂ illustrates the advantages of using a multifunctional configuration in which the photocatalyst exposes metal nanoparticles and chemically active oxide nanoparticles to the reacting water. Thus, the water molecules can interact with specific sites of the oxide nanoparticles, metal sites, and metal–oxide interfaces.

5. WO_x/TiO₂(110)

5.1. Properties of WO₃/TiO₂

Tungsten oxide exhibits interesting electronic and chemical properties that make this material attractive for applications in catalysis and photocatalysis. The optical properties of tungsten–oxide-based materials have been the subject of scientific curiosity for almost two centuries.¹⁰² WO₃ supported on other oxides (SiO₂, Al₂O₃, TiO₂, ZrO₂, MoO₃, etc.) are catalysts for isomerization of light (C₄–C₆) alkanes, various olefin conversions, alcohol dehydration, oxidation of SO₂, and selective reduction of NO_x species in exhaust gases.^{103–108} Much of the characterization effort has been focused on materials such as WO_x/Al₂O₃ and WO_x/TiO₂.^{103,106,108,109} At small loads of WO_x the oxide overlayer is anchored on the titania and alumina surfaces forming two-dimensional structures which combine WO₅ and WO₄ units.^{110,106} These structures contain oxo W=O groups and W–O–W bridges. At large coverages, the oxide overlayer coalesces to form WO₃ crystallites.^{103,106} In these systems, the coverage of WO₃ usually has a strong effect in the catalytic activity of WO₃/TiO₂. Figure 25 shows the activities of WO₃/TiO₂ catalysts for selective photocatalytic reduction of NO with NH₃ (photo-SCR).¹¹¹ N₂ was the main product (>99%), and a trace amount of N₂O was detected in the photo-SCR over all WO₃/TiO₂ catalysts. The increase in WO₃ content up to 1.5 wt % monotonously increased the photo-SCR activity (NO conversion, 79%; N₂ selectivity, 100%).

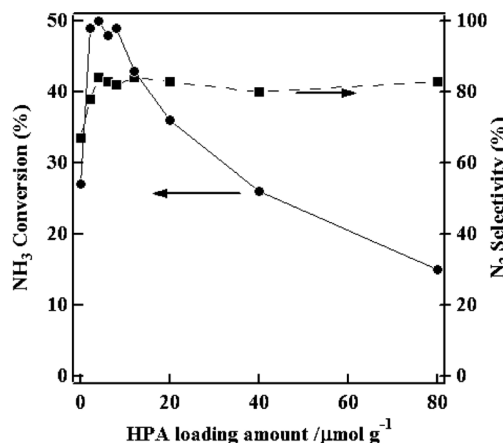


Figure 25. Selective photocatalytic reduction of NO with NH₃ on WO₃/TiO₂: Effect of WO₃ loading.¹¹¹

selectivity, 100%). The active phase of the catalyst involved octahedral WO₃ species dispersed on the TiO₂ substrate.¹¹¹ The complex nature of the surface in WO₃/TiO₂ powders makes difficult a detailed exploration of the mechanism for photocatalysis.

5.2. Isolated WO₃ Trimmers on TiO₂(110)

A procedure has been developed at Pacific Northwest National Laboratory to prepare monodispersed cyclic (WO₃)₃ clusters supported on TiO₂(110) with the goal of carrying fundamental catalytic studies. Preparation consists of sublimation of WO₃ directly onto a rutile TiO₂ crystal.¹² Low doses of WO₃ produce isolated clusters, shown in Figure 26, which are suggested to be binded to the TiO₂(110) substrate in two Ti_{5c} sites and one pointing toward an O_b as described in the scheme in the bottom of Figure 26. The tilt structure resulting from this configuration gives the contrast on the bright features observed on the STM images, with the atom pointing toward the O_b row being significantly brighter than the other two. The authors proposed originally the bonding between neighboring cationic Ti_{5c} and terminal oxygen atoms on adjacent W atoms of the trimer,^{12,112} and later carried theoretical studies which suggested binding between W(+6) ions of the cluster and O_b's of the TiO₂(110).¹¹³ The final structure that emerged from the sum of the studies involves bonding between neighboring cationic Ti⁴⁺ and terminal oxygen atoms on adjacent W atoms of the trimer. (WO₃)₃ clusters are strongly bonded to TiO₂(110)¹² and have oxo W=O groups and W–O–W bridges in a different configuration than the one observed on powder samples. Monodispersed clusters with a well-defined structure are an excellent platform for model catalytic studies.¹¹⁴

It was reported that (WO₃)₃ clusters supported on TiO₂(110) are efficient dehydration catalysts for alcohols, which utilizes both strong Lewis acid W⁶⁺ sites and W=O groups.¹¹⁴ Adsorption of 2-propanol on (WO₃)₃/TiO₂(110) is shown to produce propene, CH₃CH=CH₂, and water as the main reaction products. The W=O bonds of the mixed-metal oxide are the primary reaction sites. Experimental studies indicate that C–O bond cleavage is the rate-determining step. In TPD, H₂O desorption closely follows the propene desorption, indicating that C–H bond cleavage participates in the same transition state. Figure 27 shows the reported energy potential diagram for catalytic dehydration of 2-propanol over (WO₃)₃ clusters.¹¹⁴ The barriers for the computed steps are in

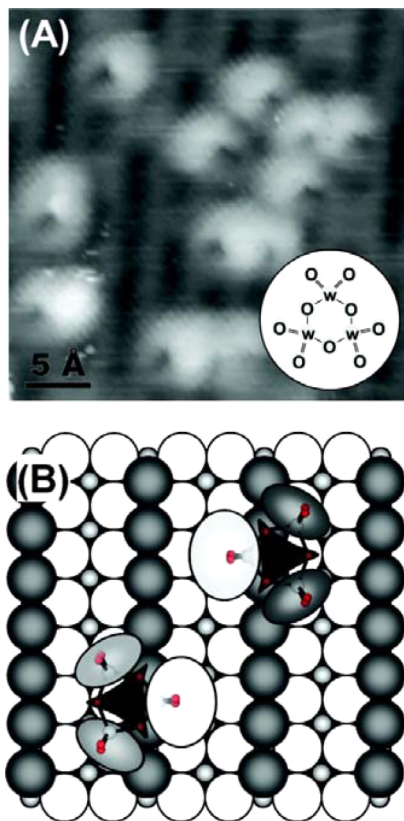


Figure 26. (A) High-resolution empty state ($+1.5$ V, 0.1 nA) STM image of 0.29 nm^{-2} of cyclic $(\text{WO}_3)_3$ clusters on $\text{TiO}_2(110)$. Clusters were deposited at 300 K and annealing at 600 K . (B) Schematic view of the $\text{TiO}_2(110)$ surface with $(\text{WO}_3)_3$ clusters. (Ti_{5c} ions are represented by small gray circles, bridging oxygen ions, Ob , by large gray circles, and second layer oxygen by large white circles.) Both $(\text{WO}_3)_3$ clusters have the ring plane tilted, with two W^{6+} ions pointing toward the Ti_{5c} row and the third W^{6+} ions tilted up and pointing toward the Ob row. This tilt results in a different brightness of the three W^{6+} ions in the cluster with the top one being significantly brighter than the other two.¹¹⁰

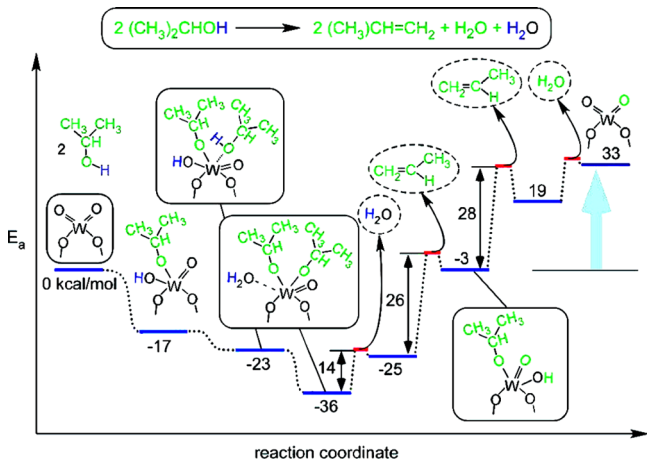


Figure 27. Calculated potential energy diagram for catalytic dehydration of two molecules of 2-propanol over $(\text{WO}_3)_3$ clusters deposited on $\text{TiO}_2(110)$ (taken from ref 114).

good agreement with the experimental observations. The initial adsorption of two alcohol molecules is barrierless and significantly exothermic. The lowest energy configuration in

the diagram corresponds to deprotonation of both alcohols. All subsequent steps are endothermic. The rate-limiting step involves rupture of the C–O bond of the propoxy with simultaneous transfer of the β -H from a methyl group. The particular configuration of the $(\text{WO}_3)_3$ clusters determines the energetics for the dehydration process. The supported $(\text{WO}_3)_3$ is an extremely efficient catalyst for dehydrogenation of alcohols, effectively lowering the energy barrier as much as possible for an endothermic reaction. The mechanism for alcohol dehydration could apply to more complex supported high surface area tungsten trioxide catalysts with the $\text{W}=\text{O}$ bonds being the primary reaction sites.¹¹⁴

Polymerization of formaldehyde has been observed on the model $(\text{WO}_3)_3/\text{TiO}_2(110)$ catalyst.¹¹⁰ The formaldehyde oligomers, $(\text{H}_2\text{CO})_n$, desorbing from the polymer formed on the mixed-metal oxide surface were detected in TPD between 250 and 325 K . The presence of H_2CO multilayers was required for polymerization, indicating that it had to occur below 100 K . Large exposures at 200 K did not result in polymerization, even though this temperature is below the $(\text{H}_2\text{CO})_n$ desorption. The amount of desorbing $(\text{H}_2\text{CO})_n$ increased with increasing H_2CO coverage but saturated for H_2CO coverages of $\sim 30\text{ ML}$, see Figure 28. The saturation

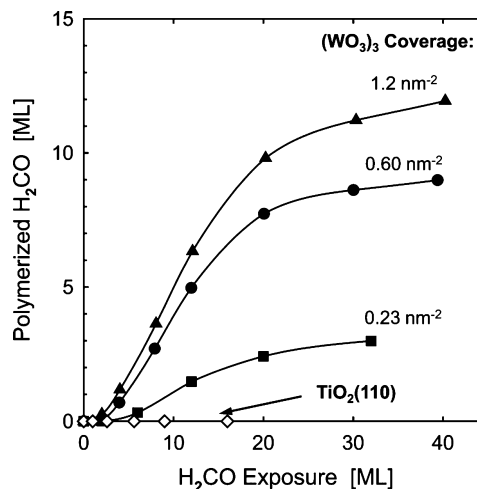


Figure 28. Amount of $(\text{H}_2\text{CO})_n$ desorption as a function of the initial H_2CO coverage and amount of $(\text{WO}_3)_3$ on the $\text{TiO}_2(110)$ surface.¹¹⁰

amount increased with increasing coverage of $(\text{WO}_3)_3$ clusters with the highest amount of 13 ML observed on $1.2\text{ }(\text{WO}_3)_3/\text{nm}^2$ as shown in Figure 28. No $(\text{H}_2\text{CO})_n$ desorption was observed on the bare $\text{TiO}_2(110)$ surface.¹¹⁰ On the basis of their work, the authors suggested two possible mechanisms: in the first mechanism, the initiation step occurs via interactions of H_2CO carbon with the $\text{W}=\text{O}$ Lewis base oxygen, while in the second mechanism the initiation step occurs via interactions of the H_2CO oxygen with the $\text{W}=\text{O}$ Lewis acid tungsten. In both mechanisms, the argument is that the presence of $\text{W}=\text{O}$ groups on the surface is the necessary condition for the polymerization process.¹¹⁰ A very recent DFT study has proposed that on reduced TiO_2 surfaces, charge transfer to $(\text{WO}_3)_3$ clusters can easily occur.¹¹⁵ The resulting charged clusters can activate chain polymerization of formaldehyde with very low activation barriers, allowing kinetic control of the polymerization reaction reaction at low temperatures, as observed experimentally.¹¹⁵

6. CONCLUSIONS

Studies of catalytic processes on well-defined mixed-metal oxide surfaces can provide an unparalleled understanding of structure–reactivity relationships. Through an effective combination of experiment and theory, these simple models can provide a conceptual framework for modifying or controlling the chemical properties of mixed-metal oxides and engineering industrial catalysts. In this respect, fundamental studies involving well-defined mixed-metal oxides can be very useful for suggesting the best ways to improve the performance of existing catalysts and accelerate the time for deployment of novel catalysts.

Deposition of nanoparticles and clusters of VO_x , RuO_x , CeO_x , and WO_x on $\text{TiO}_2(110)$ usually produces novel structures, not seen in the bulk materials, that have special chemical properties. The electronic properties of the supported oxide nanoparticles change due to size effects but also as a consequence of strong interactions with the titania substrate. Even in the case of RuO_2 on TiO_2 , when one has two oxides that like to adopt similar crystal structures, the supported oxide nanoparticles have chemical properties that are quite different from those seen in bulk phases. A major challenge is to find combinations of mixed oxides that remain stable under particular reaction conditions, where the chemical properties of the stabilized new structures give rise to more efficient heterogeneous catalysts, similar to the effect shown in this review on mixed oxides supported on titania. We expect that as we advance our fundamental understanding on the field, new families of supported mixed oxides will be deployed. From these studies it is clear that substantial benefits can be expected if one optimizes the oxide phase in metal/oxide catalysts.

AUTHOR INFORMATION

Corresponding Author

*Fax: 1-631-344-5815. E-mail: rodriguez@bnl.gov.

Notes

The authors declare no competing financial interest.

Biographies



Dario Stacchiola is an Associate Chemist at Brookhaven National Laboratory and Adjunct Professor at Michigan Technological University. He obtained his B.S. degree (1997) at UNSL (Argentina) and Ph.D. degree (2002) at the University of Wisconsin—Milwaukee and was a Humboldt Research Fellow at the Fritz-Haber-Institute in Berlin (2005–2007). His research interest is in Surface Chemistry, in particular on the structure–reactivity relationships in catalysis.



Sanjaya D. Senanayake received his B.Tech. degree (Materials) with Honors in 2001 and Ph.D. degree in Chemistry in 2006 from The University of Auckland in New Zealand. After postdoctoral work with Oak Ridge National Lab and Brookhaven National Laboratory he is at present an Assistant Scientist in the Department of Chemistry at Brookhaven National Laboratory. He also serves as the beamline scientist at X7B at the National Synchrotron Light Source.



Ping Liu is a staff scientist in the Chemistry Department and Center for Functional Nanomaterials at Brookhaven National Laboratory (BNL). She graduated from Jilin University in 2000 with a Ph.D. in Condensed Matter Physics. From 2000 to 2002 she was a postdoctoral fellow at the Technical University of Denmark. Since 2002, she has been working at BNL. Her research has focused on theoretical description of nanostructures and surfaces and their catalytic applications in cleaning of conventional oil-derived fuels, production, conversion, and utilization of nonconventional fuels such as hydrogen and ethanol.



Jose A. Rodriguez did part of his education at Simon Bolivar University in Venezuela, where he received B.S. degrees in Chemistry and

Chemical Engineering and a M.S. degree in Theoretical Chemistry. He moved to the United States to obtain his Ph.D. degree in Physical Chemistry at Indiana University, Bloomington. He is currently a Senior Scientist at Brookhaven National Laboratory and an Adjunct Professor in the Department of Chemistry of SUNY Stony Brook. Nowadays, he is involved in the preparation and study of nanocatalysts utilized for production of clean fuels and control of environmental pollution.

ACKNOWLEDGMENTS

Many of the studies described above were done in collaboration with members of the Catalysis Group at Brookhaven National Laboratory and collaborators from the Universidad Central de Venezuela, the University of Barcelona, the University of Seville, and the CSIC Institute of Catalysis in Madrid: S. Agnoli, L. Barrio, A. Bruix, J. Ciston, M. Estrella, J. Evans, J. Fernandez-Sanz, J. L. G. Fierro, J. Graciani, I. D. Gonzalez, J. Hanson, J. Hrbek, F. Illas, S. Kundu, S. Ma, R. M. Navarro, J.-B. Park, P. J. Ramirez, F. Yang, A. Vidal, and W. Wen. Many thanks to all of them. Work carried out at Brookhaven National Laboratory was supported by the U.S. Department of Energy (Chemical Sciences Division, DE-AC02-98CH10886).

REFERENCES

- (1) Thomas, J. M. *Thomas, W. J. Principles and Practice of Heterogeneous Catalysis*; VCH: New York, 1997.
- (2) Slack, A. V. Holliden, G. A. *Sulfur Dioxide Removal from Waste Gases*, 2nd ed.; Noyes Data Corp.: Park Ridge, NJ, 1975.
- (3) Pieplu, A.; Saur, O.; Lavalle, J.-C.; Legendre, O.; Nedez, C. *Catal. Rev.-Sci. Eng.* **1998**, *40*, 409.
- (4) *Catalysis by Ceria and Related Materials*; Trovarelli, A., Ed.; Imperial College Press: London, 2002.
- (5) Carreon, M. A.; Gulians, V. V. *Eur. J. Inorg. Chem.* **2005**, *27*.
- (6) Muylaert, I.; Van Der Voort, P. *Phys. Chem. Chem. Phys.* **2009**, *11*, 2826.
- (7) Ozensoy, E.; Peden, C. H. F.; Szanyi, J. *J. Catal.* **2006**, *243*, 149.
- (8) Lee, E. L.; Wachs, I. E. *J. Phys. Chem. C* **2008**, *112*, 20418.
- (9) Rodriguez, J. A. *Catal. Today* **2003**, *85*, 177.
- (10) Lee, S.; Zajac, G. W.; Goodman, D. W. *Top. Catal.* **2006**, *38*, 127.
- (11) Agnoli, S.; Sambi, M.; Granozzi, H.; Castellarin-Cudia, C.; Surnev, S.; Ramsey, M. G.; Netzer, F. P. *Surf. Sci.* **2004**, *562*, 150.
- (12) Bondarchuk, O.; Huang, X.; Kim, J.; Kay, B. D.; Wang, L.-S.; White, J. M.; Dohnálek, Z. *Angew. Chem., Int. Ed.* **2006**, *45*, 4786.
- (13) Baron, M.; Abbot, H.; Bondarchuk, O.; Stacchiola, D.; Uhl, A.; Shaikhutdinov, S.; Freund, H.-J.; Popa, C.; Ganduglia-Pirovano, M. V.; Sauer, J. *Angew. Chem., Int. Ed.* **2009**, *48*, 8006.
- (14) Wachs, I. E. *Catal. Today* **2005**, *100*, 79.
- (15) Park, J. B.; Graciani, J.; Evans, J.; Stacchiola, D.; Ma, S.; Liu, P.; Nambu, A.; Sanz, J. F.; Hrbek, J.; Rodriguez, J. A. *Proc. Natl. Acad. Sci. U.S.A.* **2009**, *106*, 4975.
- (16) Park, J. B.; Graciani, J.; Evans, J.; Stacchiola, D.; Senanayake, S. D.; Barrio, L.; Liu, P.; Sanz, J. F.; Hrbek, J.; Rodriguez, J. A. *J. Am. Chem. Soc.* **2010**, *132*, 356.
- (17) Miyasaka, S.; Amano, K.; Nojima, M.; Owari, M.; Nihei, Y. *Surf. Interface Anal.* **2008**, *40*, 1650.
- (18) Stacchiola, D.; Kaya, S.; Weissenrieder, J.; Kuhlenbeck, H.; Shaikhutdinov, S.; Freund, H. J.; Sierka, M.; Todorova, T. K.; Sauer, J. *Angew. Chem., Int. Ed.* **2006**, *45*, 7636.
- (19) Boscoboinik, J. A.; Yu, X.; Yang, B.; Fischer, F. D.; Włodarczyk, R.; Sierka, M.; Shaikhutdinov, S.; Sauer, J.; Freund, H. J. *Angew. Chem., Int. Ed.* **2012**, *51*, 6005.
- (20) Tejua, L. G.; Fierro, J. L. G.; Táscon, J. M. D. *Adv. Catal.* **1989**, *36*, 237.
- (21) Evans, J.; Lee, H. In *Topics in Environmental Catalysis*; Rao, S. V. Ed.; Interscience: New York, 2001; p 187.
- (22) Kung, H. H. *Transition Metal Oxides: Surface Chemistry and Catalysis*; Elsevier: Amsterdam, 1989.
- (23) Bond, G. C.; Tahir, S. F. *Appl. Catal.* **1991**, *71*, 1.
- (24) Wachs, I. E.; Routray, K. *ACS Catal.* **2012**, *2*, 1235.
- (25) Kundu, S.; Ciston, J.; Senanayake, S. D.; Arena, D. A.; Fujita, E.; Stacchiola, D.; Barrio, L.; Navarro, R. M.; Fierro, J. L. G.; Rodriguez, J. A. *J. Phys. Chem. C* **2012**, *116*, 14062.
- (26) Bruix, A.; Rodriguez, J. A.; Ramirez, P. J.; Senanayake, S. D.; Evans, J.; Park, J. B.; Stacchiola, D.; Liu, P.; Hrbek, J.; Illas, F. *J. Am. Chem. Soc.* **2012**, *134*, 8968.
- (27) Barrio, L.; Zhou, G.; Gonzalez, I. D.; Estrella, M.; Hanson, J.; Rodriguez, J. A.; Navarro, R. M.; Fierro, J. L. G. *Phys. Chem. Chem. Phys.* **2012**, *14*, 2192.
- (28) Henrich, V. E.; Cox, P. A. *The Surface Science of Metal Oxides*; Cambridge University Press: Cambridge, U.K., 1994.
- (29) Rodriguez, J. A. *Theor. Chem. Acc.* **2002**, *107*, 117.
- (30) Chiesa, M.; Paganini, M. C.; Giannello, E.; Di Valentin, C.; Pacchioni, G. *J. Mol. Catal. A: Chem.* **2003**, *204–205*, 779.
- (31) Rodriguez, J. A.; Stacchiola, D. *Phys. Chem. Chem. Phys.* **2010**, *12*, 9557.
- (32) Shapovalov, V.; Metiu, H. *J. Phys. Chem. C* **2007**, *111*, 14179.
- (33) Avdeev, V. I.; Tapilin, V. M. *J. Phys. Chem. C* **2010**, *114*, 3609.
- (34) Diebold, U. *Surf. Sci. Rep.* **2003**, *48*, 53.
- (35) Zhang, Z.; Henrich, V. E. *Surf. Sci.* **1992**, *277*, 263.
- (36) Centi, G.; Pinelli, D.; Trifiro, F. *J. Mol. Catal.* **1990**, *59*, 221.
- (37) Chary, K. V. R.; Kishan, G.; Bhaskar, T.; Sivaraj, C. *J. Phys. Chem. B* **1998**, *102*, 6792.
- (38) Biener, J.; Bäumer, M.; Madix, R. J. *Surf. Sci.* **1999**, *432*, 178.
- (39) Sambi, M.; Della Negra, M.; Granozzi, G. *Thin Solid Films* **2001**, *400*, 26.
- (40) Asaduzzaman, A. M.; Krüger, P. *J. Phys. Chem. C* **2008**, *112*, 4622.
- (41) Wainwright, M. S.; Foster, N. R. *Catal. Rev.* **1979**, *19*, 211.
- (42) Martinez-Huerta, M. V.; Fierro, J. L. G.; Bañares, M. A. *Catal. Commun.* **2009**, *11*, 15.
- (43) Li, M.; Altman, E. I. *J. Phys. Chem. C* **2009**, *113*, 2798.
- (44) Biener, J.; Baumer, M.; Wang, J.; Madix, R. J. *Surf. Sci.* **2000**, *450*, 12.
- (45) Agnoli, S.; Castellarin-Cudia, C.; Sambi, M.; Surnev, S.; Ramsey, M. G.; Granozzi, G.; Netzer, F. P. *Surf. Sci.* **2003**, *546*, 117.
- (46) Sambi, M.; Della Negra, M.; Granozzi, G. *Surf. Sci.* **2000**, *470*, L116.
- (47) Della Negra, M.; Sambi, M.; Granozzi, G. *Surf. Sci.* **2000**, *461*, 118.
- (48) Guo, Q.; Lee, S.; Goodman, D. W. *Surf. Sci.* **1999**, *437*, 38.
- (49) Madix, R. J.; Biener, J.; Bäumer, M.; Dinger, A. *Faraday Discuss.* **1999**, *114*, 67.
- (50) Sambi, M.; Sangiovanni, G.; Granozzi, G.; Parmigiani, F. *Phys. Rev. B* **1997**, *55*, 7850.
- (51) Chang, Z.; Piligkos, S.; Møller, P. *J. Phys. Rev. B* **2001**, *64*, 165410.
- (52) Wang, Q.; Madix, R. J. *Surf. Sci.* **2001**, *474*, L213.
- (53) Wong, G. S.; Concepcion, M. R.; Vohs, J. M. *Surf. Sci.* **2003**, *526*, 211.
- (54) Surnev, S.; Ramsey, M. G.; Netzer, F. P. *Prog. Surf. Sci.* **2003**, *73*, 117.
- (55) Magg, N.; Giorgi, J. B.; Schroeder, M.; Bäumer, M.; Freund, H.-J. *J. Phys. Chem. B* **2002**, *106*, 8756.
- (56) Biener, J.; Bäumer, M.; Madix, R. J.; Liu, P.; Nelson, J.; Kendelewicz, T.; Brown, G. E. *Surf. Sci.* **1999**, *441*, 1.
- (57) Wong, G. S.; Concepcion, M. R.; Vohs, J. M. *J. Phys. Chem. B* **2002**, *106*, 6451.
- (58) Vohs, J. M.; Feng, T.; Wong, G. S. *Catal. Today* **2003**, *85*, 303.
- (59) Feng, T.; Vohs, J. M. *J. Catal.* **2004**, *221*, 619.
- (60) Wong, G. S.; Kragten, D. D.; Vohs, J. M. *J. Phys. Chem. B* **2001**, *105*, 1366.
- (61) Amouyal, E.; Keller, P.; Moradpour, A. *J. Chem. Soc., Chem. Commun.* **1980**, 1019.

- (62) Houskova, V.; Stengl, V.; Bakardjieva, S.; Murafa, N.; Tyrpekl, V. *App. Catal. B: Environ.* **2009**, *89*, 613.
- (63) Ohno, T.; Tanigawa, F.; Fujihara, K.; Izumi, S.; Matsumura, M. *J. Photochem. Photobiol. A: Chem.* **1999**, *127*, 107.
- (64) Bikondoa, O.; Pang, C. L.; Ithnin, R.; Muryn, C. A.; Onishi, H.; Thornton, G. *Nat. Mat.* **2006**, *5*, 189.
- (65) Kundu, S.; Vidal, A. B.; Yang, F.; Ramírez, P. J.; Senanayake, S. D.; Stacchiola, D.; Evans, J.; Liu, P.; Rodriguez, J. A. *J. Phys. Chem. C* **2012**, *116*, 4767.
- (66) Yang, F.; Kundu, S.; Vidal, A. B.; Graciani, J.; Ramírez, P. J.; Senanayake, S. D.; Stacchiola, D.; Evans, J.; Liu, P.; Sanz, J. F.; Rodriguez, J. A. *Angew. Chem., Int. Ed.* **2011**, *50*, 10198.
- (67) Takakugasi, S.; Fukui, K.; Nariyuki, F.; Iwasawa, Y. *Surf. Sci.* **2003**, *523*, 41.
- (68) Onishi, H.; Iwasawa, Y. *Phys. Rev. Lett.* **1996**, *76*, 791.
- (69) Assmann, J.; Narkhede, V.; Breuer, N. A.; Muhler, M.; Seitsonen, A. P.; Knapp, M.; Crihan, D.; Farkas, A.; Mellau, G.; Over, H. *J. Phys.: Condens. Matter* **2008**, *20*, 184017.
- (70) Gao, F.; Wang, Y.; Cai, Y.; Goodman, D. W. *Surf. Sci.* **2009**, *603*, 1126.
- (71) Valden, M.; Lai, X.; Goodman, D. W. *Science* **1998**, *281*, 1647.
- (72) Zhou, G.; Hanson, J.; Gorte, R. *App. Catal. A: Gen.* **2008**, *335*, 153.
- (73) Andersson, D. A.; Simak, S. I.; Skorodumova, N. V.; Abrikosov, I. A.; Johansson, B. *Appl. Phys. Lett.* **2007**, *90*, 031909.
- (74) Zhou, G.; Shah, P. R.; Kim, T.; Fornasiero, P.; Gorte, R. *J. Catal. Today* **2007**, *123*, 86.
- (75) Wyckoff, R. W. G. *Crystal Structures*, 2nd ed.; Wiley: New York, 1964.
- (76) Rodriguez, J. A.; Ma, S.; Liu, P.; Hrbek, J.; Evans, J.; Perez, M. *Science* **2007**, *318*, 1757.
- (77) Castellarin-Cudia, C.; Surnev, S.; Schneider, G.; Podlucky, R.; Ramsey, M. G.; Netzer, F. P. *Surf. Sci.* **2004**, *554*, L120.
- (78) Rodriguez, J. A.; Graciani, J.; Evans, J.; Park, J. B.; Yang, F.; Stacchiola, D.; Senanayake, S. D.; Ma, S. G.; Perez, M.; Liu, P.; Sanz, J. F.; Hrbek, J. *Angew. Chem., Int. Ed.* **2009**, *48*, 8047.
- (79) Rodriguez, J. A.; Hrbek, J. *Surf. Sci.* **2010**, *604*, 241.
- (80) M Baron, M.; Bondarchuk, O.; Stacchiola, D.; Shaikhutdinov, S.; Freund, H. *J. Phys. Chem. C* **2009**, *113*, 6042.
- (81) Table 9: In *Lange's Handbook of Chemistry*, 13th ed.; Dean, J. A., McGraw-Hill: New York, 1985.
- (82) Graciani, J.; Plata, J. J.; Sanz, J. F.; Liu, P.; Rodriguez, J. A. *J. Chem. Phys.* **2010**, *132*, 104703.
- (83) Rodriguez, J. A.; Evans, J.; Graciani, J.; Park, J.-B.; Liu, P.; Hrbek, J.; Sanz, J. F. *J. Phys. Chem. C* **2009**, *113*, 7364.
- (84) Park, J. B.; Conner, S. F.; Chen, D. A. *J. Phys. Chem. C* **2008**, *112*, 5490.
- (85) Rodriguez, J. A.; Liu, P.; Hrbek, J.; Evans, J.; Perez, M. *Angew. Chem., Int. Ed.* **2007**, *46*, 1329.
- (86) Nakamura, J.; Campbell, J. M.; Campbell, C. T. *J. Chem. Soc., Faraday Trans.* **1990**, *86*, 2725.
- (87) Burch, R. *Phys. Chem. Chem. Phys.* **2006**, *8*, 5483.
- (88) Gokhale, A. A.; Dumesic, J. A.; Mavrikakis, M. *J. Am. Chem. Soc.* **2008**, *130*, 1402.
- (89) Flaherty, D. W.; Yu, W. Y.; Pozun, Z. D.; Henkelman, G.; Mullins, C. B. *J. Catal.* **2011**, *282*, 278.
- (90) Vayssilov, G. N.; Lykhach, Y.; Migani, A.; Staudt, T.; Petrova, G. P.; Tsud, N.; Skala, T.; Bruix, A.; Illas, F.; Prince, K. C.; Matolin, V.; Neyman, K. M.; Libuda, J. *Nat. Mater.* **2011**, *10*, 310.
- (91) Bruix, A.; Migani, A.; Vayssilov, G. N.; Neyman, K. M.; Libuda, J.; Illas, F. *Phys. Chem. Chem. Phys.* **2011**, *13*, 11384.
- (92) Vajda, S.; Winans, R. E.; Elam, J. W.; Lee, B. D.; Pellin, M. J.; Seifert, S.; Tikhonov, G. Y.; Tomczyk, N. A. *Top. Catal.* **2006**, *39*, 161.
- (93) Heiz, U.; Sanchez, A.; Abbet, S.; Schneider, W. D. *Chem. Phys.* **2000**, *262*, 189.
- (94) Tauster, S. J. *J. Acc. Chem. Res.* **1987**, *20*, 389.
- (95) Gonzalez, I. D.; Navarro, R. M.; Wen, W.; Marinkovic, N.; Rodriguez, J. A.; Rosa, F.; Fierro, J. L. G. *Catal. Today* **2010**, *149*, 372.
- (96) Fernandez-Garcia, M.; Martinez-Arias, A.; Hanson, J. C.; Rodriguez, J. A. *Chem. Rev.* **2004**, *104*, 4063.
- (97) Linsebigler, A. L.; Lu, G. Q.; Yates, J. T. *Chem. Rev.* **1995**, *95*, 735.
- (98) Trovarelli, A. *Catal. Rev.* **1996**, *38*, 439.
- (99) Gonzalez, I. D.; Navarro, R. M.; Wen, W.; Marinkovic, N.; Rodriguez, J. A.; Rosa, F.; Fierro, J. L. G. *Catal. Today* **2010**, *149*, 372.
- (100) Primo, A.; Marino, T.; Corma, A.; Molinari, R.; Garcia, H. J. *Am. Chem. Soc.* **2011**, *133*, 6930.
- (101) Kubacka, A.; Fernandez-Garcia, M.; Colon, G. *Chem. Rev.* **2012**, *112*, 1555.
- (102) Hjelm, A.; Granqvist, C. G.; Wills, J. M. *Phys. Rev. B* **1996**, *54*, 2436.
- (103) Vermaire, D. C.; van Berge, P. C. *J. Catal.* **1989**, *116*, 309.
- (104) Hilbrig, F.; Göbel, H. E.; Knözinger, H.; Schmelz, H.; Lengeler, B. *J. Phys. Chem.* **1991**, *95*, 6973.
- (105) Scheithauer, M.; Graselli, R. K.; Knözinger, H. *Langmuir* **1998**, *14*, 3019.
- (106) Eibl, S.; Gates, B. C.; Knözinger, H. *Langmuir* **2001**, *17*, 107.
- (107) Lee, J. S.; Yoon, J. W.; Halligudi, S. B.; Chang, J. S.; Jhung, S. H. *Appl. Catal. A: Gen.* **2009**, *366*, 299.
- (108) Kim, D. S.; Ostromecki, M.; Wachs, I. E. *J. Mol. Catal.* **1996**, *106*, 93.
- (109) Lebarbier, V.; Clet, G.; Houalla, M. *J. Phys. Chem. B* **2006**, *110*, 22608.
- (110) Kim, J.; Kay, B. D.; Dohnalek, Z. *J. Phys. Chem. C* **2010**, *114*, 17017.
- (111) Yamazoe, S.; Hitomi, Y.; Shishido, T.; Tanaka, T. *J. Phys. Chem. C* **2008**, *112*, 6869.
- (112) Kim, J.; Bondarchuk, O.; Kay, B. D.; White, J. M.; Dohnalek, Z. *Catal. Today* **2007**, *120*, 186.
- (113) Zhu, J.; Jin, H.; Chen, W. J.; Li, Y.; Zhang, Y. F.; Ning, L. X.; Huang, X.; Ding, K. N.; Chen, W. K. *J. Phys. Chem. C* **2009**, *113*, 17509.
- (114) Kim, Y.-K.; Rousseau, R.; Kay, B. D.; White, J. M.; Dohnalek, Z. *J. Am. Chem. Soc.* **2008**, *130*, 5059.
- (115) Di Valentin, C.; Rosa, M.; Pacchioni, G. *J. Am. Chem. Soc.* **2012**, *134*, 14086.